Challenges to equatorial plasma bubble and ionospheric scintillation short-term forecasting and future aspects in East and Southeast Asia

Guozhu Li[1,2,3,4*], Baiqi Ning[1,2,3], Yuichi Otsuka[5], Mangalathayil Ali Abdu[6], Prayitno Abadi[7], Zhizhao Liu[8], Luca Spogli[9,10], and Weixing Wan[1,2,3,4]

[1] Key Laboratory of Earth and Planetary Physics, Institute of Geology and Geophysics, Chinese Academy of Sciences, Beijing, China.
[2] Beijing National Observatory of Space Environment, Institute of Geology and Geophysics, Chinese Academy of Sciences, Beijing, China.
[3] Innovation Academy for Earth Science, Chinese Academy of Sciences, Beijing, China.
[4] College of Earth and Planetary Sciences, University of Chinese Academy of Sciences, Beijing, China.
[5] Institute for Space-Earth Environmental Research, Nagoya University, Nagoya, Japan.
[6] Divisão de Aeronomia, Instituto Nacional de Pesquisas Espaciais, São Paulo, Brazil.
[7] Space Science Center, Indonesian National Institute of Aeronautics and Space (LAPAN), Bandung, Indonesia.
[8] Department of Land Surveying and Geo-Informatics, The HongKong Polytechnic University, Hong Kong, China.
[9] Istituto Nazionale di Geofisicae Vulcanologia, Rome, Italy.
[10] SpacEarth Technology, Rome, Italy.
*Corresponding author: Guozhu Li (gzlee@mail.iggcas.ac.cn)

Abstract

Equatorial plasma bubbles (EPBs) can cause rapid fluctuations in amplitude and phase of radio signals traversing the ionosphere, and in turn produce serious ionospheric scintillations and disrupt satellite-based communication links. Whereas numerous studies on the generation and evolution of EPBs have been performed, the prediction of EPB and ionospheric scintillation occurrences still remains unresolved. The generalized Rayleigh-Taylor (R-T) instability has been widely accepted as the physical mechanism responsible for the generation of EPBs. But how the factors, which seed the development of R-T instability and control the dynamics of EPBs and resultant ionospheric scintillations, change on a short-term basis are not clear. In the East and Southeast Asia, there exist significant differences in the generation rates of EPBs at closely located stations for example Kototabang (0.2°S, 100.3°E) and Sanya (18.3°N, 109.6°E), indicating that the decorrelation distance of EPB generation is small (hundreds of kilometers) in longitude. In contrast, after the initial generation of EPBs at one longitude, they can drift zonally more than 2000 km and extend from the magnetic equator to middle latitudes of 40° or higher under some conditions. These features make it difficult to identify the possible seeding sources for the EPBs and to accurately predict their occurrence, especially when the onset locations of EPBs are far outside the observation sector. This paper presents a review on the current knowledge of EPBs and ionospheric scintillations in the East and Southeast Asia, including their generation mechanism and occurrence morphology, and discusses some unresolved issues related to their short-term forecasting, including 1) what factors control the generation of EPBs, its day-to-day variability and storm-time behavior, 2) what factors control the evolution and lifetime of EPBs, and 3) how to accurately determine ionospheric scintillation from EPB measurements. Special focus is given to the whole process of the EPB generation, development and disruption. The current observing capabilities, future new facilities and campaign observations in the East and Southeast Asia in helping to better understand the short-term variability of EPBs and ionospheric scintillations are outlined.

Keywords

Ionospheric scintillation, equatorial plasma bubble, short term variability, the East and Southeast Asia

1 Introduction

Equatorial plasma bubble (EPB) is a type of large-scale magnetic field-aligned structures featured by plasma density depletion relative to the background ionosphere, which is initially generated at the bottomside of ionospheric F region over the magnetic equator (Kelley, 2009). Its growth leads to the formation of various ionospheric irregularities, whose typical scale sizes are effective in creating diffraction of radio signals and resulting in rapid fluctuations in the signal amplitude, phase, propagation and polarization, i.e., ionospheric scintillations (e.g., Basu S. and S. Basu, 1981; Bhattacharyya, 1990; Wernik et al., 2003). The composite of the EPB and associated smaller scale irregularities are widely referred to as the equatorial spread-F (ESF), or convective ionospheric storm (Kelley, 2009). Since the early studies on radio wave scintillations in the very high frequency-ultra high frequency (VHF-UHF) band (e.g., Aarons, 1982; Liang et al., 1994), a close relationship between the occurrences of EPBs and severe ionospheric scintillations at different radio bands has been observed at low latitudes (e.g., Alfonsi et al., 2011; Spogli et al., 2016; Xiong et al., 2016).

EPBs pose serious threats to trans-ionospheric radio signals, with various consequences in communication and navigation. Kelly et al. (2014) reported that the outage of UHF satellite-helicopter communication link in Afghanistan on 4 March 2002 could be linked to the occurrence of EPBs. Concerning navigation, the reliability of Global Navigation Satellite System (GNSS) service is seriously challenged by the presence of EPBs, causing tens of meters or more deviations away from the correct position (e.g., Kintner et al., 2001). Under strong scintillations caused by EPBs, the amplitude of GNSS signal fading can be up to more than 25 dB that can disrupt GNSS receivers' carrier tracking loop to satellite channels, causing loss-of-lock of GNSS signals, decrease of the amount of available GNSS satellites for positioning, and communication/navigation failures (e.g., Seo et al., 2009; Zhang et al., 2010; Spogli et al., 2016). Since the GNSS signals have been widely used in many applications of modern high technology society, the need for forecasting the occurrences of EPB and ionospheric scintillation, and mitigating their effects becomes more important than ever. Despite some attempts have been made to predict GNSS scintillations at low latitudes (e.g., Rezende et al., 2010; Alfonsi et al., 2017; Grzesiak et al., 2018), a final word is far to be told.

Leveraging on a variety of techniques based on observations like Total Electron Content (TEC) and scintillation indices from GNSS receiver, echoes from ionosonde, coherent and incoherent scatter radars, airglow imaging, and in-situ observations from Low-Earth Orbit satellite instruments, EPB and associated irregularities have been widely investigated (Kelley, 2009; Woodman, 2009, and the references therein). One prominent feature of the EPB structure as revealed from previous studies is that the EPB depletion can penetrate the F layer peak onto the topside ionosphere, also extending along the magnetic field lines to low, even middle latitudes. By making use of the Jicamarca radar observations, a backscatter plume structure starting at F region bottomside and extending 600 km altitude was reported by Woodman and La Hoz (1976). From observations of two-dimensional maps of backscatter echoes by the ALTAIR radar, together with simultaneous satellite in-situ measurements of plasma density, Tsunoda (1981) showed that the radar backscatter plumes were related to the EPBs with deep plasma density bite outs and very steep boundaries. Using the all-sky airglow imager observation over Sata (31.0ºN, 130.7ºE) and over its near conjugate station Darwin (12.4ºS, 131.0ºE), Otsuka et al. (2002) reported similar structures of EPB depletions simultaneously detected by the two imagers, demonstrating thereby that EPBs are depleted plasma density

structures elongated along the magnetic field lines to low latitudes over both hemispheres. Whereas most of the EPBs are confined within the equatorial and low latitude regions, there are a few cases of super plasma bubble and strong scintillation events reported to have occurred at middle latitudes of 40°N or higher in some longitude sectors during geomagnetic storms (e.g., Ma et al., 2006; Sahai et al., 2009; Li et al., 2009a, 2018a; Katamzi-Joseph et al., 2017; Aa et al, 2018), indicating that the EPB depletion structures could reach an apex altitudes as high as 3400 km or more over the magnetic equator.

In the zonal (east-west) direction, the width of an EPB depletion may vary from tens to hundreds of kilometers. Statistical results from the Ion Velocity Meter (IVM) measurements onboard the Communications/ Navigation Outage Forecasting System (C/NOFS) satellite showed that the widths of EPBs could vary from 110 km to 460 km, with a prominent peak occurring around 200 km. The absence of smaller scale EPB structures was caused by the median filter employed in the processing of plasma density data from the IVM (Smith and Heelis, 2017). Observations from ground-based airglow imagers show that the widths of EPBs due to the seeding of small-scale wave structure (Liu et al., 2019) and of bifurcated EPBs (Shiokawa et al., 2004) can be down to tens of kilometers, about 70 km and 50 km, respectively. Whereas the widths of EPBs are generally on the order of hundreds of kilometers, they may affect a large longitudinal sector of thousand kilometers due to their zonal drifts, which are strongly driven by the thermospheric zonal winds that are usually eastward under geomagnetic quiet conditions (e.g., Muella et al., 2017). The Kototabang (0.2°S, 100.3°E) and Sanya (18.3°N, 109.6°E) radar campaign observations in the East and Southeast Asia showed that EPBs could drift zonally more than 2000 km away from their onset longitude (Li et al., 2013).

Whereas the general features of EPBs and their medium term variability have been well understood, the factors controlling the day-to-day and shorter term variabilities of the EPB and scintillation occurrences are still not clear (e.g., Abdu, 2001, 2019; Yamamoto et al., 2018). In the East and Southeast Asia, the seasons of high and low probability of EPB occurrences are equinoctial and solstitial months, respectively. However, observations have shown that the EPBs might be absent (present) on some nights of equinoctial (solstitial) months. Under similar ionospheric background conditions, for example, under the same upward vertical plasma drift of the F layer, EPBs do not always occur during consecutive days of equinoctial months (e.g., Tsunoda et al., 2010; Li et al., 2012). On the other hand, during June solstitial months, EPBs have been observed occasionally (e.g., Ajith et al., 2018; Carter et al., 2018; Otsuka, 2018). The main difficulties for the predictability of EPBs and ionospheric scintillations concern the following questions: (1) What factors control the generation of EPBs and how the controlling factors change on a day-to-day basis? (2) What factors control the evolution and lifetime of EPBs, since the zonally drifting EPBs may contribute to the hourly variability of the EPBs over a given longitude? (3) How to accurately determine ionospheric scintillation from EPB measurements? In this paper, we present a review on our current knowledge of EPB and ionospheric scintillation occurrences over the East and Southeast Asia, and discuss some unresolved issues related to their predictability, with special focus on the observation of EPB from its generation to disappearance. To track the whole process of EPBs, campaign observations with multiple ionospheric networks in the East and Southeast Asia are proposed. Future aspects on the ionospheric facilities being planned or built to better understand the short term variability of EPB and scintillation are included.

2 General mechanisms of EPB and ionospheric scintillation

The generation of EPBs has been well accepted as resulting from the generalized Rayleigh–Taylor (R-T) instability (Kelley, 2009). The linear growth rate of R-T instability (γ) depends

on the F region upward vertical plasma drift (V) by $E\times B/B^2$ due to the eastward electric field (E), the upward neutral wind perpendicular to the magnetic field (U), the ion-neutral collision frequency (v_{in}), the plasma density gradient scale length (L), the recombination rate (β), the E and F region field-line-integrated conductivity (Σ_p^E, Σ_p^F), and is given as (Sultan, 1996),

$$\gamma = (1/L)\times\frac{\Sigma_p^F}{\Sigma_p^E+\Sigma_p^F}\times(V - U + g/v_{in}) - \beta,$$

A steep upward density gradient, which is antiparallel to gravity g, usually exists at F region bottomside over the magnetic equator. During daytime, the conductivity in the low latitude E region (Σ_p^E) is very high (due to solar radiation), and can short out the F region polarization electric fields and thus suppress the growth of the R-T instability. The EPBs are difficult to be generated during daytime except in some unusual circumstances, such as, when a plasma density perturbation structure with extremely large density gradient is created by artificial sources (Li et al., 2018b). The radar beam steering measurements over Kototabang have shown that almost all EPB plumes are generated after sunset over the magnetic equator (Yokoyama et al., 2004). After sunset, there is no photoionization in the ionosphere. Charged particles at lower altitudes are recombined quickly, resulting in higher altitude of the F layer and smaller scale length of the density gradient (L). The E region conductivity decreases drastically after sunset, causing a large conductivity gradient in the zonal direction near the sunset terminator. To maintain the divergence-free condition of the electric currents, the zonal component of F region electric field often increases to a large eastward value, which is known as the pre-reversal enhancement of the eastward electric field (PRE) (e.g., Eccles et al., 2015). The PRE can drive large upward vertical drifts that can elevate the F region to higher altitude of lower v_{in} and β, and thus cause larger growth rate of R-T instability.

The linear growth rate of R-T instability at nighttime, which is primarily controlled by F layer height and field-line-integrated conductivity, is usually less than 2 e-folds per hour. The growth rate is too small to explain the rapid development of EPBs after sunset (e.g., Woodman, 2009). On the other hand, Abdu et al. (2008) reported an unusual case over Brazil where very large upward plasma drifts up to ~1000 m/s were observed but without EPBs during the geomagnetic storm of October 2003. Some other factors could play important roles on the generation of EPBs. In previous numerical simulations of EPBs, an initial seeding with plasma density perturbation at the F region bottomside was studied. Whereas the seeding perturbation itself does not change the growth rate of the R-T instability, simulation results have shown that an initial perturbation ~~at~~ ~5% or so can greatly reduce the time required for the R-T instability to grow into EPBs (see a review by Yokoyama, 2017). The gravity wave launched from atmospheric convective activity in the low atmosphere, such as, in the intertropical convergence zone (ITCZ), is one possible source producing the density perturbations (see reviews by Tsunoda et al., 2018; Abdu, 2019). Some case studies suggested a possible link between the occurrences of tropical cyclone and EPB (e.g., Yang and Liu, 2016). Another possible source is the collisional shear flow in the F region bottomside, where the plasma drifts westward but the neutral wind is eastward near sunset (Hysell and Kudeki, 2004).

The scale sizes of the EPB structure are usually on the order of thousands of kilometers along magnetic field line and tens to hundreds of kilometers in the direction perpendicular to magnetic field line. Such large-scale structures cannot explain the concurrent ionospheric scintillations and radar backscatter plume echoes. The amplitude scintillation index S_4, which has been widely used in the study of ionospheric scintillation and defined as the normalized variation of signal intensity (Yeh and Liu, 1982), is given by:

$$S_4 = \sqrt{(<I^2> - <I>^2)/<I>^2},$$

where I is the signal intensity, <> means the ensemble average. The intensity of scintillation depends on the radio wave frequency. The scintillation is mainly caused by the plasma density irregularities with the scale size below the first Fresnel scale (e.g., Yeh and Liu, 1982) and defined as:

$$d_F = \sqrt{2\lambda z},$$

where z is the height of irregularity layer, λ is radio wave length. For the GPS L1 frequency (1575.42 MHz), the first Fresnel scale is about 390 m (by assuming that z is 400 km). Ionospheric scintillations have been recorded by making use of the VHF/UHF to L-band satellite beacons (Basu et al., 1988), indicating that the signals traverse the irregularities with size of hundreds of meters. The radar backscatter plumes are produced from echoes due to Bragg scattering from the irregularities with the size of half the radar wavelength. Most of the ionospheric radars are operated at frequencies in the range of 30-50 MHz for detecting irregularities with the scale size of a few meters. Specifically, plasma density irregularities were also detected by X-band radars (with operational frequencies up to a few GHz) (e.g., Xu et al., 2004; Mohanty et al., 2018), indicating that the size of irregularities can be down to a few centimeters. The observations demonstrate that within the EPBs, there exist various scale sizes of irregularities filling the whole depletion structure.

It was suggested that small-scale irregularities can be generated through the cascading process during the upward growth of EPB depletion structure (Haerendel, 1974). The polarization electric fields generated within large-scale depletion structures of EPBs can extend long distances along the magnetic field lines. It is expected that the large-scale polarization electric fields (within large-scale EPB structures) can map along magnetic field lines to produce similar large-scale structures at low latitudes of both hemispheres, as demonstrated by airglow imager observations at magnetic conjugate stations (Otsuka et al., 2002). However, for the small-scale irregularities generated within EPBs over the magnetic equator, the mapping to low latitudes is difficult because the small-scale polarization electric fields associated with the irregularities can be partially, or fully, short-circuited. LaBelle (1985) estimated the mapping efficiency of electric fields generated within different scale sizes of irregularities along magnetic field lines. For the F region irregularity structure with scale sizes larger than 10 km, the mapping efficiency of electric fields from the magnetic equator to low latitudes is more than 60%. Larger scale (for example 50 km) structure corresponds to higher mapping efficiency (~90%). For the polarization electric fields generated within smaller scale (less than 1 km) irregularities, the mapping efficiency is close to 10% or less, indicating that the small-scale polarization electric fields cannot map over long distance. The small-scale irregularities which produce radar backscatter echo plumes and ionospheric scintillations at low/middle latitudes are not due to the direct mapping of polarization electric fields generated within small-scale EPB irregularities over the magnetic equator, but generated locally through the cascading process within the large-scale depletions at low/middle latitudes.

Besides the EPB irregularities, there are two other types of irregularities which may also cause ionospheric scintillations at low/middle latitudes. These are the E region irregularities associated with the sporadic E layer and the F region irregularities generated through the Perkins instability (e.g., Alfonsi et al., 2013; Yang and Liu, 2018). The frequency-type spread-F in ionograms at mid latitudes are usually due to the irregularities generated through the Perkins instability (e.g., Xiao et al., 2009; Balan et al., 2018). For a specific propagation geometry of radio signals traversing an ionospheric irregularity structure, the scintillation intensity depends on the background ionospheric density, the thickness of irregularity structure, and the root-mean-square of electron density fluctuations ($<\Delta N^2>^{1/2}$) inside the structure (e.g.,

Yeh and Liu, 1982). EPBs often cover hundreds of kilometers or more in the east-west, north-south and altitude directions, and penetrate the F region peak onto the topside ionosphere. The background plasma density and the density gradient in the boundary of EPBs near the altitudes of F region peak are the largest. The scintillation produced by the EPB irregularities can be very strong with saturated values of S_4. However, for the other two types of irregularities that are embedded within relatively small patches or thin-layered structures, the ionospheric scintillations are usually weak and of short durations (a few minutes), and do not significantly impact on the functionalities of satellite-based communication links.

3 Occurrence morphology of post-sunset, post-midnight and daytime EPBs and ionospheric scintillations

Based on the time of occurrence, the EPBs can be classified into three categories, the post-sunset (~18-24 LT), the post-midnight (~00-06 LT) and the daytime (~06-18 LT) EPBs. Under geomagnetic quiet conditions, the EPBs are generated mainly during post-sunset hours following the vertical drift enhancement of the F region plasma (Yokoyama et al., 2004). The EPBs observed during the post-midnight are usually due to the long lifetime of the EPBs generated at post-sunset hours, as shown, such as, in the statistical results of EPB occurrence obtained from a global GNSS TEC receiver network (Li et al., 2011). On the other hand, some post-midnight EPBs are not the continuation of post-sunset EPBs, but initially generated during midnight/post-midnight hours, especially during solar minimum years (see a review by Otsuka, 2018). The EPBs generated during midnight, or later could survive to daytime hours. Huang et al. (2012) reported a special case of EPBs that was initially observed at 0200 LT and lasted for about 12 hours to the afternoon (1400 LT). Under geomagnetic active conditions, the EPBs could be generated later in the night (even near sunrise) due to the contribution of storm time disturbed electric fields (e.g., Fukao et al., 2003). Almost all the daytime EPBs are the continuation of the EPBs generated at nighttime.

The climatological behavior of the EPB occurrences under geomagnetic quiet conditions has been well understood (e.g., Su et al., 2006). In general, the occurrence rate of the post-sunset EPBs peaks at solar maximum. At a given longitude, the post-sunset EPBs mainly occur during the months when the sunset terminator is aligned with the magnetic meridian (Abdu et al., 1981a). The longitudinal and seasonal variations of the post-sunset EPBs can be explained by the longitudinal gradient of field-line-integrated E region conductivity (Tsunoda, 1985). The amplitudes of PRE, which greatly affect the growth of R-T instability and hence the EPB generation, are sensitive to the longitudinal gradient of the field-line-integrated E region conductivity. A good correspondence between the seasonal variations of EPBs and of plasma vertical drifts driven by the PRE was found from Jicamarca observations (Fejer et al., 1999) and from ROCSAT global observations (Li et al., 2007). Based on a comparative analysis of the EPB occurrence rates with the sunset vertical plasma drifts, a linear relationship was found for all seasons (e.g., Kil et al., 2009). Statistical results from the C/NOFS data during 2008-2013 showed that the EPB occurrence rates get very close to 100% when the upward vertical plasma drifts driven by PRE are more than 40 m/s (Huang and Hairston, 2015; Huang, 2018).

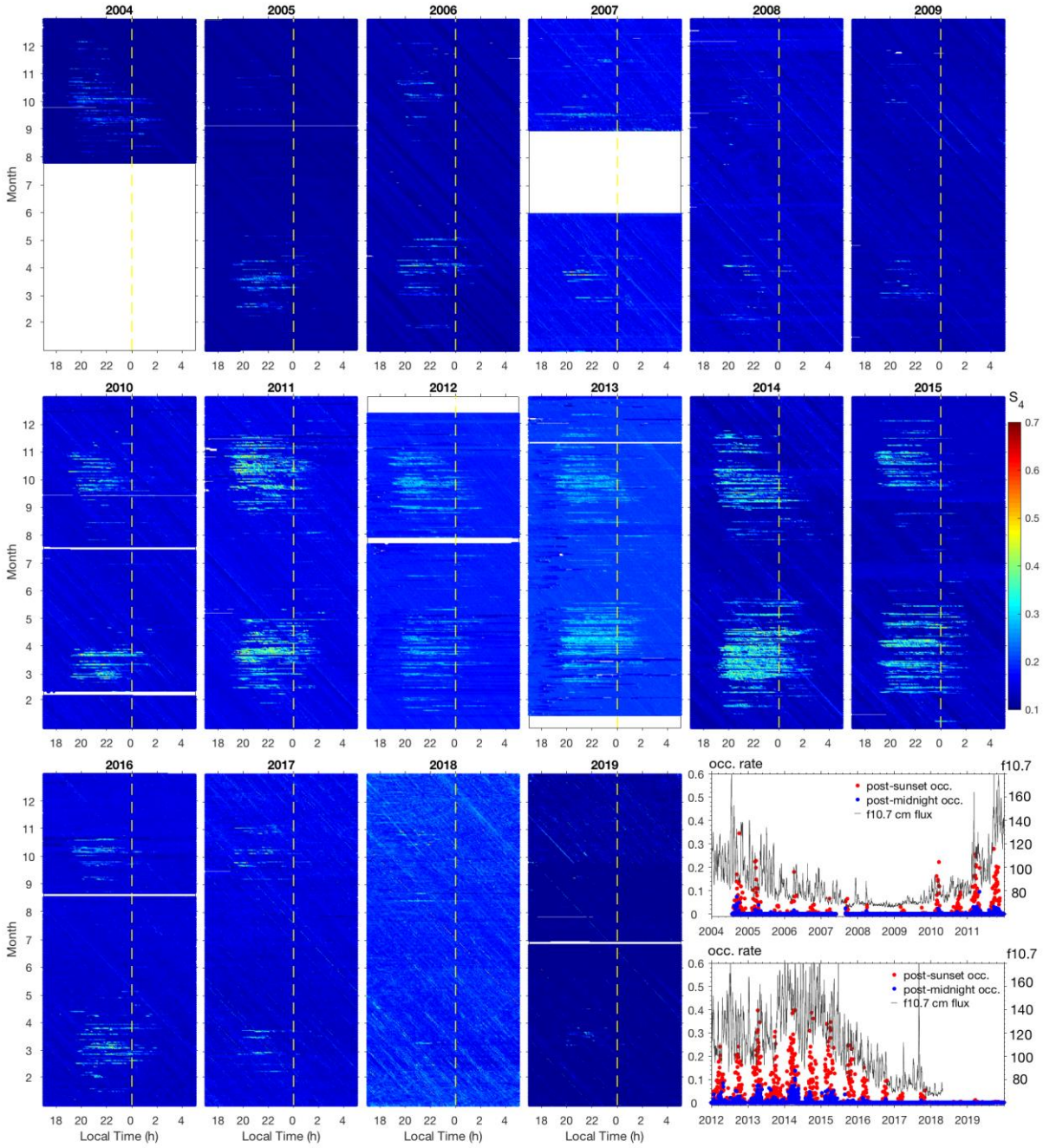

Figure 1. The occurrence morphology of GPS ionospheric scintillations observed over the low latitude station Sanya during 2004-2019. The vertical dashed lines superimposed in the color plots represent the midnight. The slant stripes are due to multipath effect. The right bottom two panels show the variations of solar 10.7 cm flux (black line), and post-sunset (red dots) and post-midnight scintillation occurrence rates (blue dots) as a function of time (date). The post-sunset and post-midnight occurrence rates are defined as the number of data points with S_4>0.2 divided by the total number of data points (for all GPS satellites with elevation> 25º) during 18-24 LT and 00-06 LT on each day, respectively. Note that in 2018 and 2019, the occurrence rates are almost 0%, indicating that the threshold of 0.2 is appropriate for removing the possible contamination by multipath effect (which is apparent in 2018) in the statistics.

Over East and Southeast Asia, the magnetic declination angle is very small (~1°) and the magnetic equator offset from the geographic equator does not vary much with longitude. Large PRE and high EPB occurrence rates are expected during the equinoctial months (March, April,

September and October) when the E region sunset at low latitudes of both hemispheres occur at roughly the same time with the apex sunset over the magnetic equator. Previous observations from the low latitude stations in the East and Southeast Asia showed that the EPB occurrence maximized in the equinoctial months (e.g., Shi et al., 2011; Buhari et al., 2017). At post-sunset hours, the EPBs are usually in the development phase, during which they are composed of various scale sizes of irregularities, which can contribute to ionospheric scintillations. The scintillations in the East and Southeast Asia are mainly equinoctial phenomena (e.g., Liu et al., 2015; Tran et al., 2017).

Figure 1 shows the local time, seasonal and solar activity dependences of amplitude scintillations measured by GPS scintillation receiver at the low latitude station Sanya. All the S_4 values are observed with elevation angles greater than 25° and 1-min interval, but only the maximum S_4 are plotted in Figure 1. It is evident from the figure that ionospheric scintillation mainly occurs at post-sunset hours during equinoctial months of solar maximum. With the decrease (increase) in solar flux, the scintillation intensity correspondingly decreases (increases). The scintillation was rarely observed in the low solar flux years 2008–2009 and 2018-2019. The right bottom two panels show the variations of post-sunset and post-midnight scintillation occurrence rates and of 10.7cm solar flux as a function of time (date). At solar maximum year, the occurrence rate of post-sunset scintillation can be up to 40% on some days, indicating that during the period, 40% of satellite-receiver links could be affected by scintillations over Sanya.

Unlike the post-sunset EPBs/ionospheric scintillations which are positively correlated with solar activity and have similar longitudinal/seasonal patterns for high and low solar activities, the occurrences of post-midnight EPBs and scintillations show complex behavior. The post-midnight EPBs do not always cause ionospheric scintillations, which depend on the change of total electron density (e.g., Huang et al., 2014). At the solar maximum, the longitudinal/seasonal variations of post-midnight EPBs are similar to those of post-sunset EPBs except the relatively low occurrence rate. This can be explained by the fact that the post-midnight EPBs are mostly the continuation of EPBs generated at post-sunset. However, at the solar minimum, the occurrence rate of post-midnight EPBs which can be higher than that of post-sunset EPBs over some longitude sectors, has different longitudinal/seasonal dependences. The equatorial ionogram spread-F observations at the American, Pacific, and Southeast Asian longitudinal sectors during the June solstice of solar minimum show a higher occurrence rate of irregularities in midnight/post-midnight than post-sunset (Li et al., 2011). Observations from the C/NOFS and Swarm satellites show that post-midnight EPBs appeared mainly during June solstice with an occurrence peak in the African sector, where post-midnight VHF scintillations were also recorded by ground-based receivers (e.g., Yizengaw et al., 2013; Wan et al., 2018). In the Asian sector, an enhanced occurrence of post-midnight irregularities was observed at low latitude stations Gadanki, Kototabang and Sanya during June solstice of solar minimum but without concurrent GPS scintillations (e.g., Otsuka et al., 2009; Patra et al., 2009; Hu et al., 2014). As can be seen from Figure 1, in general, no obvious scintillations were observed at Sanya near midnight/post-midnight during the June solstice of solar minimum. A reason for this could be that the midnight/post-midnight background electron density is low. The changes of total electron density by irregularities are small and thus may not produce apparent scintillations.

In the case of post-midnight irregularities observed at low latitudes, the echoing patterns in radar range-time-intensity (RTI) maps may present mid-latitude characteristics at times (Yokoyama et al., 2011). These post-midnight irregularities could be generated locally through

the Perkins instability. On the other hand, the simultaneous observations at equatorial and low latitudes present evidence that some of the low latitude post-midnight irregularities could be linked with the EPBs freshly generated through the R-T instability mechanism operating in the midnight/post-midnight hours (e.g., Otsuka et al., 2009; Patra et al., 2009; Li et al., 2011; Yizengaw et al., 2013; Hu et al., 2014; Dao et al., 2017). As described above, the generation of EPBs requires positive growth rate for the R-T instability, which is proportional to the F layer height. The statistical results from the equatorial ionosonde observations at different longitudes during June solstice of solar minimum show that post-midnight irregularities are mostly preceded by substantial height rise of F region near midnight (Li et al., 2011; Nishioka et al., 2012). Upward vertical plasma drifts driven by eastward electric fields around midnight are also detected by satellite in-situ observations (Yizengaw et al., 2013). The height rise/upward drift provides favorable conditions for the growth of R-T instability since the ion-neutral collision frequency decreases with increasing altitude. The meridional neutral wind associated with midnight temperature maximum in the thermosphere was suggested to be another possible cause for the midnight F layer uplift (Otsuka, 2018).

During daytime, the presence of EPB is not a common phenomenon. Satellite in-situ observations show that the density fluctuations caused by any daytime EPBs are usually small. The longitudinal, seasonal and solar activity dependences of daytime EPBs are still not clear. The daytime EPBs mainly appear at the F region topside, and are related to the long lifetime of the EPBs initially generated at nighttime (Huang et al., 2012). One possibility responsible for the long time survival of the EPBs during daytime is the relatively low plasma production rate in the daytime F region topside. The occurrence rate of the EPBs during daytime decreases gradually from morning to afternoon hours (Kil et al., 2019). Radar observations at equatorial and low latitudes in the American and Southeast Asian sectors also show that daytime F region backscatter echoes are only sporadically observed, with durations of 1-2 hours in RTI map and extremely narrow Doppler spectral widths (e.g., Chau and Woodman, 2001; Chen et al., 2017). Since the radar observations are confined to limited longitude/latitude regions and limited periods of time, it is not clear if the daytime F region backscatter echoes result from the daytime EPBs surviving from nighttime, and how often these daytime echoes appear. A further investigation on the daytime F region backscatter echoes is worth of a future work leveraging on beam steering measurements with multiple radars at closely located longitudes. On the other hand, the fresh generation of daytime F region EPB-like irregularities was observed at low latitudes following the creation of a big ionospheric hole by rocket exhausts (Li et al., 2018b). Both the freshly generated as well as the decayed daytime F region irregularities were not accompanied by ionospheric scintillations. The spatial scale and/or intensity of the daytime F region irregularities may not be favorable for scintillation.

4 Unresolved issues in the EPB and the ionospheric scintillation short-term forecasting

The controlling factors and associated physical mechanisms responsible for the climatological characteristics of EPB occurrence, including the longitudinal, seasonal and solar activity dependences, are well understood. This may enable the development of predictive capability on long-term variability of EPB occurrence at any longitude, for example the monthly forecasting of ionospheric scintillation achieved with the WideBand MODel (WBMOD) in the East and Southeast Asia (e.g., Cervera et al., 2001). However, the factors that explain well the long term variability cannot be used to reliably predict the day-to-day and shorter term variations in the EPB occurrence rates, which have small decorrelation distances in longitudes (see reviews by Tsunoda et al., 2018; Abdu, 2019). Considering that the longitudinal extent of the PRE covers ~30° (~3000 km in the east-west direction), it may be expected that the generation of the EPBs over a large longitude region could have similar features. However, the

radar observations at Kototabang and Sanya which are separated by ~1000 km in longitude show a large difference of EPB generation rates. The significantly higher EPB generation rate over Kototabang was suggested to be linked with the more active ITCZ near the Kototabang longitude, where the gravity wave activity could be more frequent resulting in more intense seeding and the development of the R-T instability (Li et al., 2016). Whereas the generation rates are significantly different, the bubble occurrences which include both zonally drifting and locally generated EPBs over the two longitudes are similar. To forecast EPBs and ionospheric scintillations over a given longitude, it is essential to determine if EPBs will be generated locally, or EPBs will be generated at elsewhere and travel into the given longitude through zonally drifting, and if EPBs will cause ionospheric scintillation. Correspondingly, the main questions on the predictability of EPBs and ionospheric scintillations lie in three aspects: (1) what factors control the generation of EPBs and how the controlling factors change on a day-to-day basis, (2) what factors control the evolution and lifetime of EPBs, and (3) how to accurately determine ionospheric scintillation from EPB measurements.

4.1 The factors controlling the EPB generation and its day-to-day variability

The EPB generation is primarily determined by the factors including (1) the plasma density perturbation (wave structure in the east-west direction) at F region bottomside for seeding the R-T instability, (2) the equatorial vertical plasma drift and F layer height, and (3) the field-line-integrated conductivity controlling the growth rate of the R-T instability (see reviews by Abdu, 2001, 2019). McClure et al. (1998) explained the generation of EPBs (P_{EPB}) as a product of two occurrence probabilities, that is, $P_{EPB}=P_{seed}P_{inst}$, where P_{seed} and P_{inst} represent the probabilities of perturbation seeding and of R-T instability, respectively. Under the condition when one probability is small but the other probability is high, it may also work effectively to generate EPBs. The day-to-day variability of EPBs depends on the variations of both P_{seed} and P_{inst}, which arise from different sources.

The occurrence of F region bottomside plasma density perturbation (P_{seed}) can be directly detected by the steerable incoherent scatter radar (e.g., Tsunoda, 2005) and all-sky airglow imager (e.g., Takahashi et al., 2010; Liu et al., 2019), and indirectly derived from the 'satellite traces' in ionograms which are caused by the oblique reflections from tilted ionosphere (e.g., Abdu et al., 1981b; Tsunoda, 2008; Alfonsi et al., 2013) and from the TEC perturbations in longitude (e.g., Tulasi Ram et al., 2014). Based on the two dimensional (altitude versus east-west distance) measurements of ionospheric plasma density with the ALTAIR incoherent scatter radar, Tsunoda (2005) reported that the generation of EPBs is preceded by the presence of plasma density perturbation, representing large-scale wave structure (LSWS) at F region bottomside. The sinusoidal depletion structure of the LSWS can cover more than 1500 km in longitude, as observed by the all-sky airglow imagers at equatorial and low latitudes (Takahashi et al., 2010). The EPBs are known to develop at the crest of LSWS. Abdu et al (2009) reported that the LSWS can appear nearly simultaneously at low latitude magnetic conjugate sites.

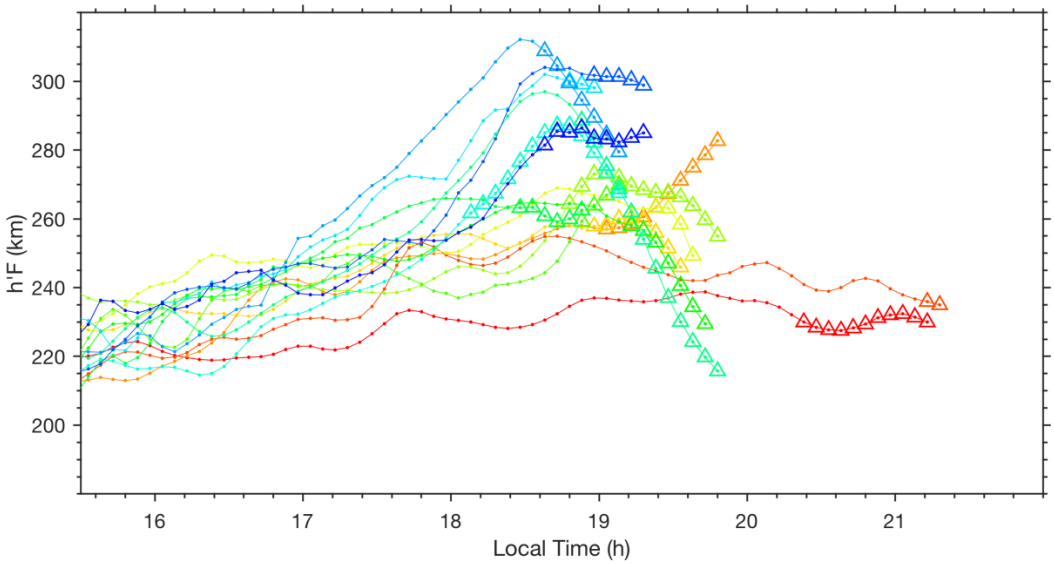

Figure 2. Cases showing the occurrences of large-scale wave structure (characterized by satellite traces in ionograms) and F layer virtual height perturbation over Sanya (updated from Li et al., 2012). The triangles denote the presence of satellite traces. The different colors denote the observations on different days.

Figure 2 shows some cases of the occurrence of satellite traces (marked with triangles) and the variations of F layer virtual heights (h'F) obtained from the low latitude ionosonde at Sanya during September-October 2011. The h'F oscillations with weak amplitude were observed during afternoon hours on some days. These oscillations, which could be linked with LSWS, are similar to those observed at low latitudes in the South America, where the observed h'F oscillations continuously existed from midday to sunset with the amplitude increasing towards sunset (Abdu et al., 2015a). Near sunset when the PRE vertical drift increases, the perturbation amplitude could be amplified (e.g., Tulasi Ram et al., 2014; Tsunoda et al., 2018) and cause satellite traces in ionograms. The amplification could be linked with the increasing field-line integrated conductivity ratio toward sunset and/or the spatial resonance mechanism of gravity waves and background drift (Huang and Kelley, 1996; Abdu et al., 2015a). Statistical results from the equatorial and low latitude observations showed that the generation of EPBs is almost always preceded by satellite traces (e.g., Tsunoda, 2010; Li et al., 2012; Patra et al., 2013; Abdu et al., 2015; Zhu et al., 2015).

The generation of the LSWS is usually attributed to the following three possible mechanisms.

1. The collisional shear instability mechanism that is believed to be driven by a velocity shear associated with the PRE near sunset. The shear flow begins in the afternoon and gets intensified near sunset when the difference between neutral wind and plasma drift velocities is on the order of 100 m/s. Hysell and Kudeki (2004) suggested that the shear flow instability can produce large scale perturbation structure at F region bottomside that could act as a seeding source for the R-T instability.

2. The gravity waves propagating upward to F region bottomside over magnetic equator might produce the LSWS. Such gravity waves could be generated due to tropospheric convective activities that are present at any time of the day. The LSWS characterized in ionogram as the 'satellite traces', which appear in the afternoon or midnight (when the shear flow is usually small) might be linked with gravity waves (e.g., Tsunoda et al., 2018). Li et al. (2016) explained the extremely large difference of EPB generation rates at closely located longitudes (in the Asian sector) as being caused partly by the gravity waves sourced in the

ITCZ. The SpreadFEx campaign (Fritts et al., 2008) observations showed a good correspondence between the horizontal wavelengths of gravity waves and the inter-bubble distances in longitude, the distances being typically more than 100 km (e.g., Takahashi et al., 2009).

3. The large-scale polarization electric fields generated by medium-scale traveling ionospheric disturbance (MSTID) at low latitudes could map along magnetic field lines to equatorial F region bottomside and produce the LSWS. Based on the SAMI3/ESF model simulation, Krall et al (2011) investigated the coupling between the low latitude MSTIDs and the EPBs. When the MSTIDs propagate in a direction nonparallel to the geomagnetic field line, the associated polarization electric fields could map to equatorial F region bottomside and produce an MSTID-like density wave, thus triggering the development of EPBs. The statistical results from the observations over the South America showed a close relationship between the inter-bubble distance and the horizontal wavelength of MSTIDs (Takahashi et al., 2018). In general, both the shear flow and gravity waves (directly or indirectly by the MSTID polarization electric field) may produce the LSWS and thus seed the development of the EPBs. However, the day-to-day variabilities that characterize the shear flow and the gravity wave are unknown, especially for gravity waves that cannot be directly observed. Also, the threshold limits set by the LSWS parameters for EPB generation are not clear because direct observation of LSWS by the steerable incoherent scatter radar is very limited.

Regarding the equatorial vertical plasma drift and F layer height, there are several possibilities that may cause its short term variability. One is the background electric fields that may be modified by other factors on a day-to-day basis. Near sunset, the PRE which drives F layer to higher altitudes can be modified by planetary/Kelvin waves, and by storm time prompt penetration electric field (PPEFs) or disturbance dynamo electric fields (DDEFs). These factors causing the day-to-day variability of PRE have been discussed in detail (see reviews by Abdu, 2012, 2019, and the references therein). The tidal winds, which affect the sunset E layer conductivity gradient and thus the PRE and F layer height variations, can be modulated by the nonlinear interactions between planetary/Kelvin waves and tidal waves (Abdu et al., 2015b). The unseasonal occurrence of post-sunset EPBs preceded by a substantial uplift of equatorial F layer on 28 July 2014 in Asia was suggested to be linked with planetary waves (Ajith et al., 2018; Carter et al., 2018). At midnight of solar minimum when the temperature maximum frequently occurs in the summer hemisphere, the weakening of westward electric field together with sufficient recombination may cause the rise of F layer height (Otsuka, 2018).

During geomagnetic storm, the F layer height can be increased at post-sunset (post-midnight) by the PPEFs (DDEFs), or decreased at post-sunset by DDEFs. That is because the polarities of PPEFs (DDEFs) are eastward (westward) at the longitudes in the dayside and westward (eastward) at the longitudes in the nightside (e.g., Abdu, 2012). Super EPBs covering from equatorial to middle latitudes in the East and Southeast Asia were detected in the geomagnetic storms of January, July and November 2004 (Sahai et al., 2009; Li et al., 2009, 2010). Strong scintillations with maximum S_4 of ~1 were recorded at the low-middle latitude station Wuhan (30.5°N,114.4°E). Especially for the storm of July 2004, the EPBs were generated continuously over a very wide range of the equatorial region, that is, more than 180° in longitude, from American to Southeast Asia sectors (Li et al., 2010). Since in these months, the EPBs, in general, seldom occur in the East and Southeast Asia, it has been suggested that long duration/multiple PPEFs contributed to the rapid elevation of F layer height, thus significantly enhancing the growth of R-T instability and the EPB development. The PPEFs, which typically occur during the main phase of magnetic storms and last for tens of minutes to 1-2 hours, if

appearing in the evening (with eastward polarity), can enhance the background upward plasma drift and thus increase~~ing~~ the EPB occurrence. A few hours after the beginning of storm main phase, the DDEFs often develop and become important during the storm recovery phase. The DDEFs, with westward (eastward) polarity in the postsunset (post-midnight) sector, can suppress or even reverse the background upward (downward) plasma drift and thus suppress~~ing~~ (increase~~ing~~) the EPB occurrence. Whereas the generation of super EPBs is usually triggered by geomagnetic storm, previous statistical results showed that the occurrence rates of EPBs are statistically inhibited by geomagnetic activity. By using TEC observations at equatorial and low latitudes in the East and Southeast Asia during 2001-2004, a decreasing of pre-midnight EPB occurrence rates with increasing magnetic activity (characterized by Kp index) was observed (Li et al., 2009b). Shinagawa et al. (2018) investigated the relationship between the daily total Kp (ΣKp) and EPB/scintillation occurrence over low latitude Kototabang during 2011-2013. A similar decrease of EPB occurrence rate with increasing ΣKp was observed. Based on numerical model simulation, Carter et al. (2014) reported that even a small change in Kp can affect (inhibit) the growth rate of R-T instability and EPB during its high occurrence season.

Another potential source for F layer height variation is gravity waves, which may produce the variations through direct or indirect ways (e.g., Abdu et al., 2009; Li et al., 2012; Joshi et al., 2015). The zonal component of gravity wave perturbation winds can modify the PRE and thus affecting F layer height. The meridional component of perturbation winds can directly affect F layer height (at latitudes away from the magnetic equator). On the other hand, the F layer height variations could be linked directly with the plasma density perturbation structure produced by gravity waves. Statistical results from Saito and Maruyama (2007) showed that the F layer height (h'F) at two equatorial stations could be quite different during the days when EPBs were observed. They suggested that the plasma density perturbation structure could cause the h'F difference. The F layer height modulation by gravity waves could be interrupted at higher altitude with the start of EPBs (for example please see the orange curve shown in Figure 2). The h'F measured overhead could depend upon the perturbation upwelling depth and zonal distance away from the crest of perturbation structure. Previous studies have shown that even when the PRE is weak, EPB can still be generated at times due to strong plasma density perturbations (e.g., Tsunoda et al., 2010). Because the h'F and vertical drift velocity on both EPB and non-EPB days at one longitude can have large scatters, it i~~'~~s difficult to determine whether or not ~~the~~ EPB occurs ~~rence or not~~ using a certain threshold of F layer height.

The ratio of F region (Σ_p^F) to the total (E and F region) field-line-integrated conductivities ($\Sigma_p^E + \Sigma_p^F$), which also controls the growth of R-T instability, can be decreased by transequatorial wind and low latitude Es layer. The transequatorial wind causes F layer height rise in one hemisphere and descend in the other hemisphere, and thereby produces opposing effects of Σ_p^F but with a larger amplitude for the decrease of Σ_p^F. As a result, it causes decrease in the ratio and growth rate (Maruyama, 1988). By employing the transequatorial winds derived from the magnetic conjugate ionosonde observations in Southeast Asia (~100°E), Maruyama et al. (2009) simulated the EPB development. Their results showed that the growth time of EPB increased by a factor two when the transequatorial wind velocity increased from 10 to 40 m/s, indicating suppression of EPB by transequatorial winds. For the Σ_p^E at low latitude E region which is connected to equatorial F region through magnetic field lines, the occurrence of low latitude Es layer can cause increase in Σ_p^E and thus decrease in the conductivity ratio. Joshi et al. (2013) reported that when blanketing type Es layer occurred at low latitude for a relatively long duration near sunset, no EPB was observed. It was suggested that the thick Es layer has

larger Σ_p^E which could reduce the growth rate of the R-T instability significantly. The increased Σ_p^E by Es layer can also slow down the rise of sunset F layer height (Carrasco et al., 2005). One general mechanism for Es layer is the tidal wind shear which can be modified also by gravity waves and planetary waves.

4.2 The factors controlling the evolution and lifetime of EPBs

After the initial generation at the bottomside of the equatorial F region, the EPBs can rise to higher altitudes extending along the magnetic field lines to low, or even middle latitudes, and drift zonally (toward east or west) for a long distance up to more than 2000 km. The rising altitude and zonally drifting distance may determine how wide an area may be affected by the EPB and the associated scintillation.

Figure 3 shows the latitudinal occurrence rates of kilometer-scale plasma irregularities derived from GNSS TEC measurements around 110°E. By using a similar method as that used by Li et al. (2009a), the rate of TEC index (ROTI), which was defined as the standard deviation of the rate of TEC change (ROT) over a five-minute window (Pi et al., 1997), was employed to estimate the occurrence rates of irregularities with a latitudinal resolution of 1° from 13°N to 40°N in the longitude region of 105-115°E. For the TEC data sampled at 30-s intervals, the scale sizes of irregularities producing significant ROTI values are on the order of a few kilometers (for example 6 km), depending on the zonal drift velocity over ionospheric pierce point (for example 100 m/s).

As shown in the left color maps of Figure 3, two types of irregularities occurring at different latitudes are identified from the ROTI measurements. One is the F region irregularities generated at middle latitudes through the Perkins instability and related with Es/MSTIDs during June solstice (Balan et al., 2018, and the references therein), as indicated by the superimposed circles. The right panels show that the middle latitude irregularities present a sub-peak of occurrence rate centering around 28-29°N. The other type is the EPB irregularities which cause the main occurrence peak at low latitudes. In general, both middle latitude irregularities and EPB (low latitude) irregularities increase with solar activity. Here we will focus only on the EPB irregularities. At solar maximum (2000-2002), most EPB irregularities were observed at latitudes up to ~25°N (assuming the irregularity altitude 300 km) which corresponded to the apex altitude of ~1050 km over the magnetic equator at 110°E. The occurrence peak of EPB kilometer-scale irregularities were situated around 17°N, instead of lower latitudes close to the magnetic equator. This is consistent with the occurrence peak of hundred meter-scale irregularities which are expected to produce ionospheric scintillation maxima near the crest of equatorial ionization anomaly (EIA) (e.g., Abadi et al., 2014). At solar minimum (2007-2009), the EPB irregularities were detected mainly at latitudes below 18°N, indicating that the peak altitudes of EPB plumes over the magnetic equator were usually less than 550 km. On the other hand, it can be noted from the color maps of Figure 3 that a few EPB irregularities were observed extending from low to middle latitudes up to 40°N or higher (as indicated by the superimposed arrows), corresponding to the apex altitude of ~3400 km over the magnetic equator at 110°E. These plasma bubble events at mid latitude occurred during the geomagnetic storms of October 2002, January, July and November 2004, and August 2005, respectively. Some of these storm time middle latitude plasma bubble cases in the East and Southeast Asia have been investigated in previous studies (e.g., Xu et al., 2007; Sahai et al., 2009; Li et al., 2009a, b, 2010). Geomagnetic activity may cause modifications in the background electric field and plasma density significant enough to provide favorable conditions for EPBs to attain higher enough altitudes and thus extending to higher latitudes.

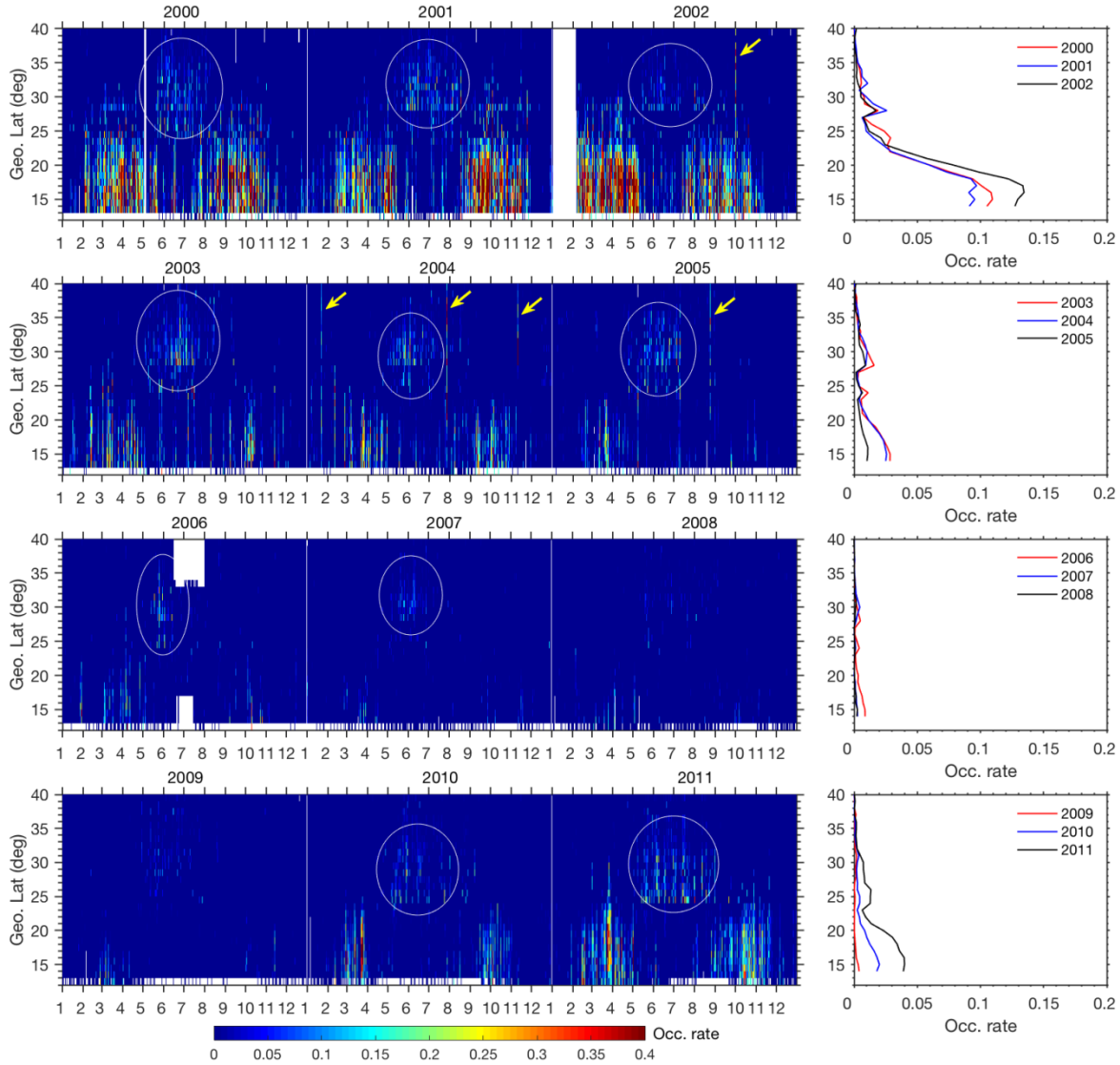

Figure 3. Latitudinal occurrence rates of F region kilometer-scale plasma irregularities derived from TEC measurements. In the left colored maps, the latitudinal occurrence rates, as a function of time (date), were calculated with the number of (ROTI-ROTI$_{avg}$) > 0.2 divided by the total number of ROTI within the grid of 10° in longitude (105-115°E) and 1° in latitude during nighttime 18-06 LT on each day. ROTI$_{avg}$ is the mean value of ROTI during the daytime 06-17 LT. The latitudinal occurrence rates shown in the right plots were calculated with the same method but using the nighttime data in the whole year. The superimposed circles and arrows in the left colored maps highlight the irregularities generated at middle latitudes during June solstice, and the storm time middle latitude plasma bubble irregularity events, respectively.

In general, the peak altitude of the EPBs depends on the field-line-integrated electron density inside the bubble and the adjacent background electron density. The vertical rise velocity determines how long the bubble could take to reach the peak altitude. The rise velocity mainly depends on the F region background zonal electric field. As suggested by Abdu et al. (1983), the background electric field can affect the rise velocity in two ways, (1) causing difference in the conductivity between the bubble and adjacent regions and thus change of polarization electric field. The eastward polarization electric field in the EPB depletion structure drives the upward drift of low-density plasma via E×B drift; and (2) uplifting the F layer to higher altitudes where the ion-neutral collision frequency becomes lower and the instability growth rate becomes larger. Based on the radar multi-beam steering observations at low latitude, Tulasi

Ram et al. (2017) reported the rise velocities of post-sunset (post-midnight) EPB structures to be around 45-265 m/s (26-128 m/s). They further simulated the rise velocity under different background electric fields using a high resolution bubble (HIRB) model (Yokoyama, 2017). When the background eastward electric field was increased from 0.5 mV/m to 1 mV/m, the vertical rise velocity increased correspondingly from 227 m/s to 264 m/s. On the peak altitude to be reached by an EPB, Mendillo et al. (2005) proposed that the upward motion of EPB will stop when the field-line-integrated electron density inside the bubble is equal to that of the adjacent background. This was confirmed by the SAMI3 model simulation (Krall et al., 2010).

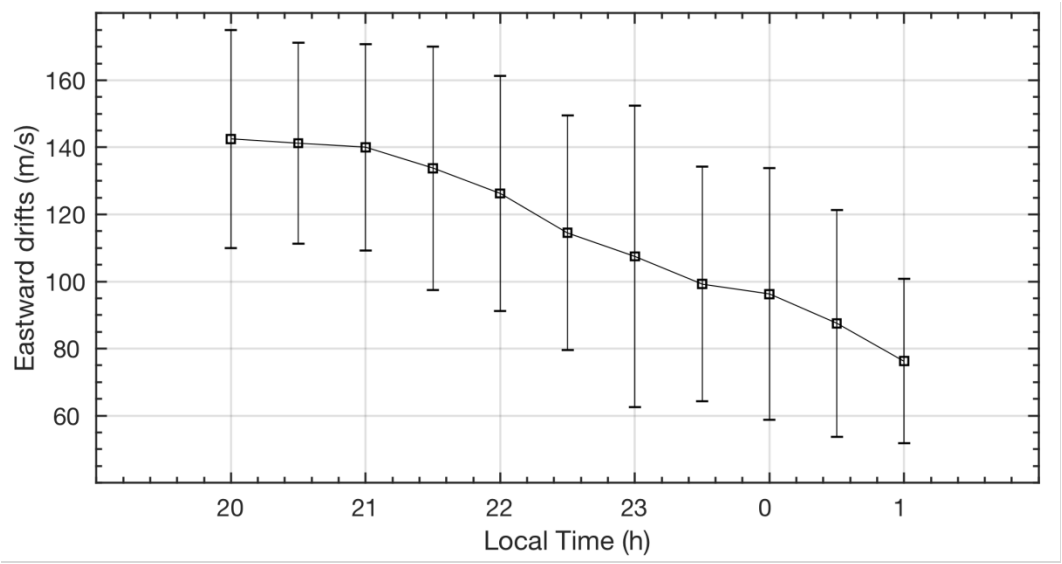

Figure 4. The mean zonal drifts (geomagnetic quiet condition with daily averaged Kp<3) of EPB irregularities derived from the measurements by spaced scintillation receivers at Sanya during the equinoctial months in 2011-2013 (updated from Liu et al., 2015).

The zonal drift distance of the EPBs could depend on the zonal drift velocity and the lifetime of EPBs. The EPBs usually drift eastward at nighttime with the velocity decreasing with increasing local time and reversing to west in the early morning hours (e.g., Bhattacharyya et al., 2001; Fejer et al., 2005). Since the EPBs are embedded in the surrounding background plasma, the zonal drift velocity of EPBs and its variation with local time and solar activity are, in general, similar to those of F region background plasma drift. For the west/east tilted EPB structure, the zonal drift of bubble structure can be larger/smaller than the background plasma drift, due to the motion of plasma particles inside the depletion structure (Huang et al., 2010). Figure 4 shows the mean zonal drift velocity derived from scintillation measurements using spaced GPS receivers operated at the low latitude station, Sanya, during 2011-2013 (a high solar activity period). The zonal drifts decrease during the period 20-01 LT from about 145 m/s to 75 m/s with an average decreasing rate of ~15 m/s/h. This is consistent with the global results from C/NOFS, which showed the velocity ranging between 130 m/s and 40 m/s during high solar flux period (Huang and Roddy, 2016). Unlike the quiet time behavior, the zonal drifts of background plasma and EPBs during geomagnetic activity could be significantly disturbed, with the eastward drifts decreasing and attaining even large westward drifts. Previous observations in the East and Southeast Asia showed that during geomagnetic storms, the EPBs have large westward drifts of ~80 m/s or more (e.g., Xu et al., 2007; Li et al., 2009a). Sometimes the westward drifts increase with latitude, causing west-tilted EPB vertical structures (Li et al., 2018a). These storm time westward drifts could be due to the PPEF-

induced Hall drifts and/or due to the disturbance induced westward thermospheric winds (Abdu, 2012).

The lifetime of the EPBs at nighttime depends mainly on the characteristics of these EPBs and the condition of background ionosphere, such as, the scale size and depletion depth of the EPB structures, and the recombination rate and plasma diffusion in the direction perpendicular to the geomagnetic field. Under similar background conditions, the EPBs with larger size and deeper depletion can survive longer. For a plasma structure with wavenumber k, the time of diffusion is given as $(k^2D)^{-1}$ (e.g., Otsuka et al., 2006; Kelley, 2009), where D is the perpendicular diffusion coefficient. For a specific D (1 m/s^2), the diffusion time of irregularity structures with scales of 1 km and 400 m are estimated approximately 7 hours and 1 hour, respectively. This can explain that during the late phase of EPB, the hundred-meter scale irregularities (which produce scintillation) decay but the kilometer scale irregularities persist. On the other hand, a larger recombination rate can cause faster decay of EPBs. Generally, the recombination rate is larger at solar maximum than at solar minimum, and larger at lower altitude than at higher altitude. Based on the C/NOFS observations at different solar activities, Huang et al. (2012) reported that the EPBs at low solar activity persisted for longer time (7 h or longer), but at high solar activity the life time was shorter, ~3 h. They suggested that the atmospheric density as well as the recombination rate, which are controlled by solar activity, might be responsible for the observed difference. The short lifetime of post-sunset EPBs at high solar activity was further thought to be linked with the rapid downward movement of F region at post-sunset hours. If we take the mean velocity (decreasing from 130 m/s to 40 m/s with a rate of ~15 m/s/h at solar maximum, and from 70 m/s to 20 m/s with a rate of ~6 m/s/h at solar minimum) and the averaged life time (3 h at solar maximum and 7 h at solar minimum), the EPBs, on average, can drift zonally by ~1250 km.

4.3 EPB measurements to determine the ionospheric scintillation

Ionospheric scintillations are induced by small-scale irregularities, i.e., below the Fresnel's scale, which are generated through secondary instabilities within the depletion structure of rising EPBs through a cascading process (Haerendel, 1974). The scintillation intensity increases with the strength of density fluctuation (ΔN) of the irregularity structure. In the East and Southeast Asia, the GPS scintillation observations showed that the occurrence peak was situated at the crest of EIA region (e.g., Abadi et al., 2014), similar to that observed in the South America (e.g., Muella et al., 2017). That is because the background plasma density and irregularity strength at the EIA crest are significantly higher than those at other latitudes. The variability of the spatial gradients along the North-South direction at the EIA crest was suggested to be a principal driver of scintillation (Cesaroni et al., 2015). Numerical model simulation results have shown that when large-scale EPB structures extended from magnetic equator to low latitudes, the ΔN is not uniform but proportional to the background plasma density along magnetic field lines (Dao et al., 2012). During geomagnetic storms when the evening EIA crests shift poleward to higher latitudes, the poleward expansion of the scintillation occurrence peak could be detected.

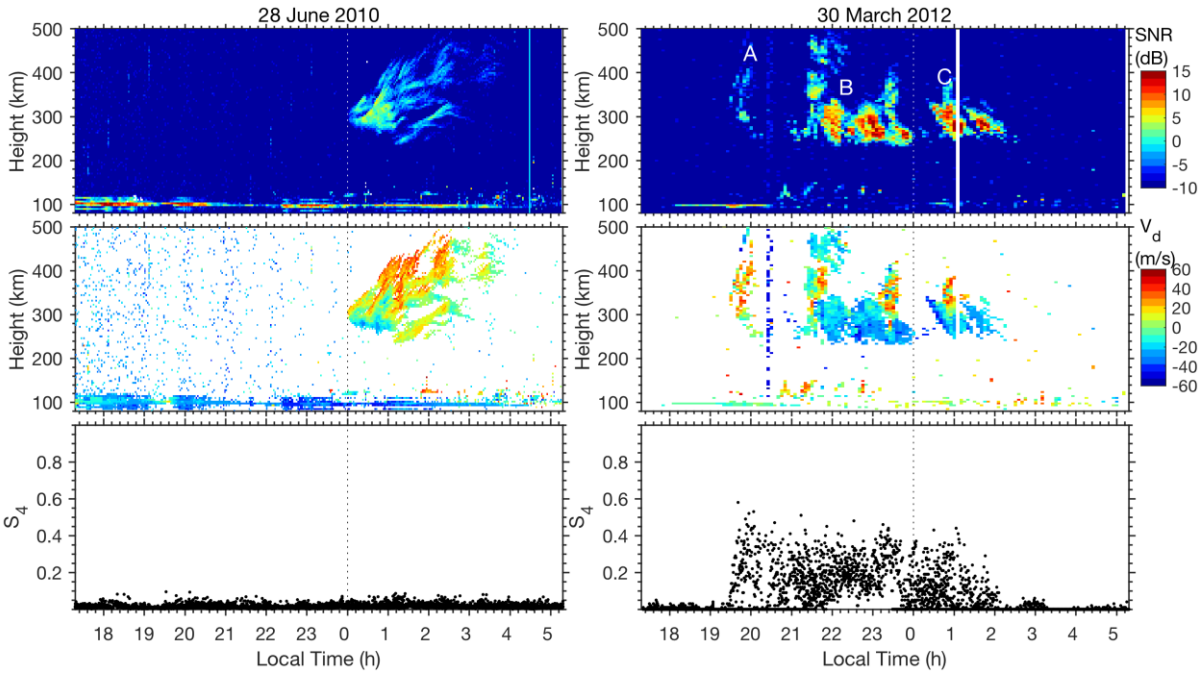

Figure 5. Cases of EPB backscatter plumes (left) without and (right) with accompanying scintillation over Sanya on 28 June 2010 and 30 March 2012, respectively. The top panels show the radar height-time-intensity maps of backscatter echoes. Three plume groups (labeled with 'A', 'B' and 'C') were observed on 30 March 2012. The middle panels show the echo Doppler velocity maps. The bottom panels show the amplitude scintillation.

In order to examine the ability of EPB measurements to determine ionospheric scintillation occurrence over the same location, the correlation between EPBs and the resulting scintillations must be quantified in the first place. The satellite and rocket in-situ data, and coherent radar backscatter echo data often show a good correlation between the occurrences of EPB depletions and backscatter plumes with S_4, whereas the irregularities probed by radar have scale sizes (a few meters) much smaller than those causing scintillations (a few hundred meters). Figure 5 shows a comparison of the EPB backscatter plumes and ionospheric scintillations over Sanya. As shown in the right top panel, three EPB groups were detected on 30 March 2012. It has been suggested that the periodic EPB structures in radar RTI map during Equinox over Sanya are caused by spatially periodic EPBs in longitude, which could drift eastward into the radar field of view successively (e.g., Li et al., 2013). The first plume group 'A' around 1930-2000 LT was generated in the eastern side of Sanya, where part of the plume structure was detected by the radar beam. The other two plume groups 'B' and 'C' were generated in the western longitudes of Sanya. The horizontal separations of periodic EPBs, usually on the order of hundreds of kilometers, are similar to the wavelengths of the LSWSs (e.g., Tsunoda, 2005; Maruyama and Kawamura, 2006; Li et al., 2012; Rodrigues et al., 2018). From the right panels of Figure 5, it can be seen that there is a good correspondence between the EPBs and scintillations during both post-sunset and post-midnight hours. In contrast, the left panels of Figure 5 show a case of EPB observed at midnight, around 00-04 LT on 28 June 2010 (solar minimum). This EPB did not cause any ionospheric scintillations. The simultaneous observation by C/NOFS (figure not shown here) indicates that this EPB was generated near midnight. For both days, the Doppler velocities of backscatter plume echoes are significantly positive, indicating that these plume irregularities are evolving. The absence of ionospheric scintillation on 28 June 2010 is possibly due to the weak irregularity intensity. The echo intensity of backscatter plumes around 00-04 LT on June 28 is mostly around ~2 dB (or less), significantly weaker than that observed at 00-02 LT on March 30 (up to 10 dB or more).

Using the simultaneous observations recorded by VHF radar and scintillation receiver at Sanya during equinoctial months of 2010-2017, we investigated the statistical relationship between the F region backscatter echo intensity at altitudes of 200-500 km and the maximum S_4 during the nighttime 1900-0500 LT. As shown in Figure 6, in general, there is a positive correlation between the backscatter echo and scintillation intensities. From the color maps, it can be seen that when the EPB irregularities cover large altitude range with large echo intensities, the corresponding scintillation is strong. The thin layered irregularities, such as, the F region bottomside/bottom-type irregularities appearing around 200-220 km in September 2015 (the top of middle panel), even with large echo intensities, did not cause ionospheric scintillation. The right bottom panel of Figure 6 shows the one-to-one relationship between the backscatter echo intensity and the scintillation index S_4. Besides the general positive relationship, there are two groups of data points (marked by the circled areas 'A' and 'B') showing different patterns, which are due to the presence of irregularity thin layer, or that the EPB irregularities causing scintillations appearing outside the field-of-view (FOV) of the radar beam. Considering the different FOVs of radar (small) and scintillation receiver (large), a further investigation on the possible threshold of EPB backscatter echo intensity for scintillation occurrence is worth of a future work leveraging on long-term radar multi-beam steering measurements.

For the EPB measurements by radar, the backscatter echo intensity can be estimated from the radar and irregularity related parameters (Costa et al., 2011):

$$\mathrm{SNR} \approx \frac{r_e^2}{32\pi^3 k_B} C_r C_m \frac{<\Delta N^2>}{r^2},$$

where r_e is the classical electron radius (2.82×10^{-15} m), k_B is the Boltzmann's constant (1.38×10^{-23} J/K), r is the vertical range, SNR is the signal-to-noise ratio, C_m represents the group of parameters of irregularity spectral shape (outer scale size, break scale size, one-dimensional and two-dimensional spectral indices), and C_r represents the groups of parameters of radar (antenna gain and radiation pattern, half-power beam width, pulse length, transmitted power and radar wavelength), propagation loss and noise temperature. It is clear that the echo intensity (SNR) is directly proportional to the mean squared electron density fluctuation $<\Delta N^2>$ divided by the squared vertical range. Larger echo intensity represents stronger density fluctuation and thus larger S_4 value, which is consistent with the observations shown in Figure 6. As the EPB structure is elongated along magnetic field lines, radar beam steering measurements in the east-west direction could provide a three-dimensional description of the irregularity strength characterized by the backscatter echo intensity, and thus estimate the scintillation information over a large region.

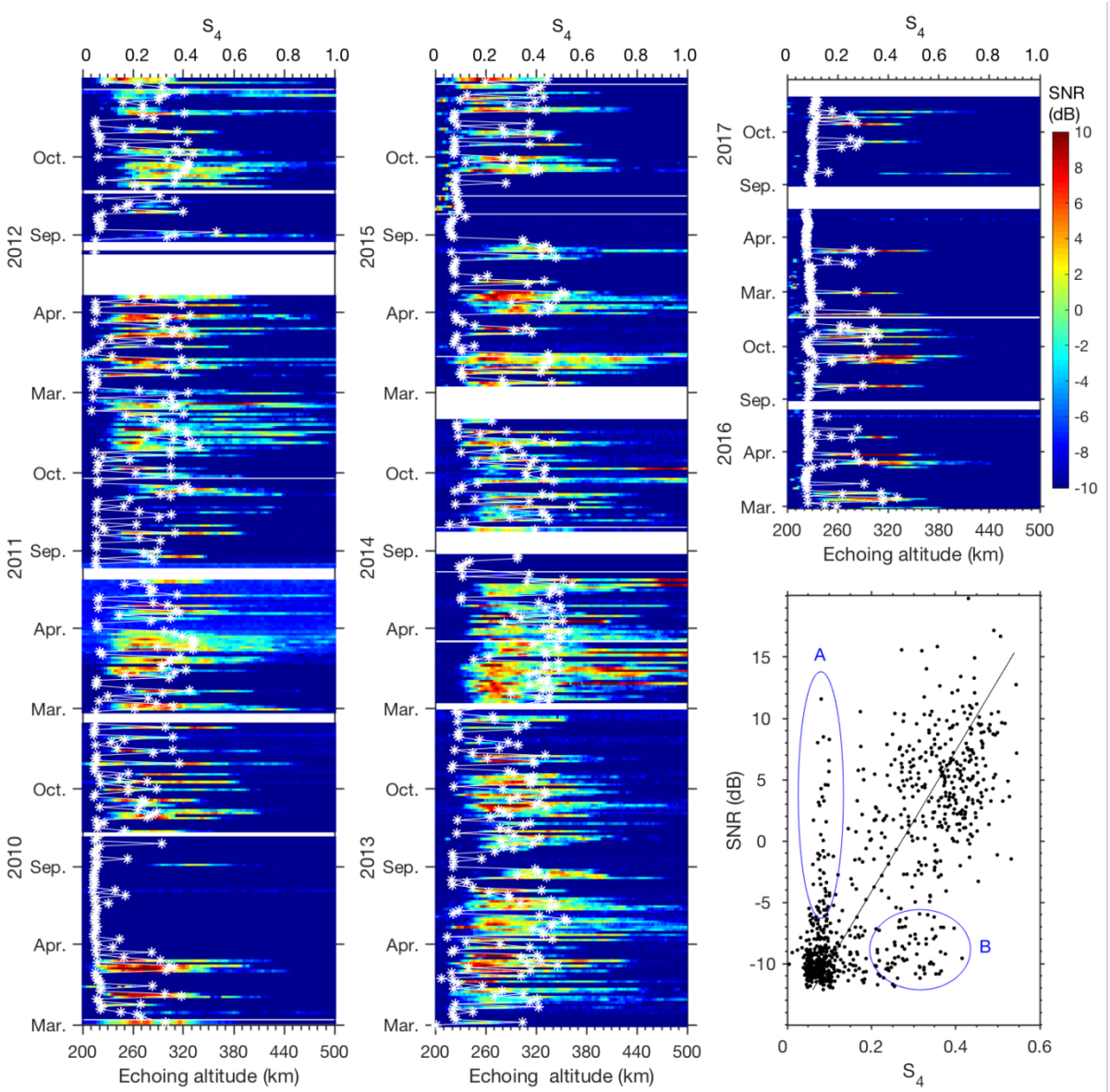

Figure 6. The relationship between the maximum backscatter echo intensity ($Echo_{max\_alt}$, color coded map) and maximum ionospheric scintillation S_4 index (S_{4max}, marked by white asterisks) during the equinoctial months (March, April, September and October) of 2010-2017. The echo intensity at each altitude bin and the scintillation intensity are averaged within 30 min interval during 1900-0500 LT. The right bottom plot, in general, shows a good positive correlation between the S_{4max} and the $Echo_{max\_alt}$ within 200-500 km altitudes. The weak scintillations with large echo intensity (marked by the circle 'A') are due to the presence of F region bottomside/bottomtype irregularities, which are usually thin layers (for example the observations in September 2015). The moderate scintillation with weak echo intensity (marked by the circle 'B') is due to the fact that the EPBs causing scintillations appeared outside the field-of-view of the radar beam (for example the scintillation only observed in the southern sky of Sanya).

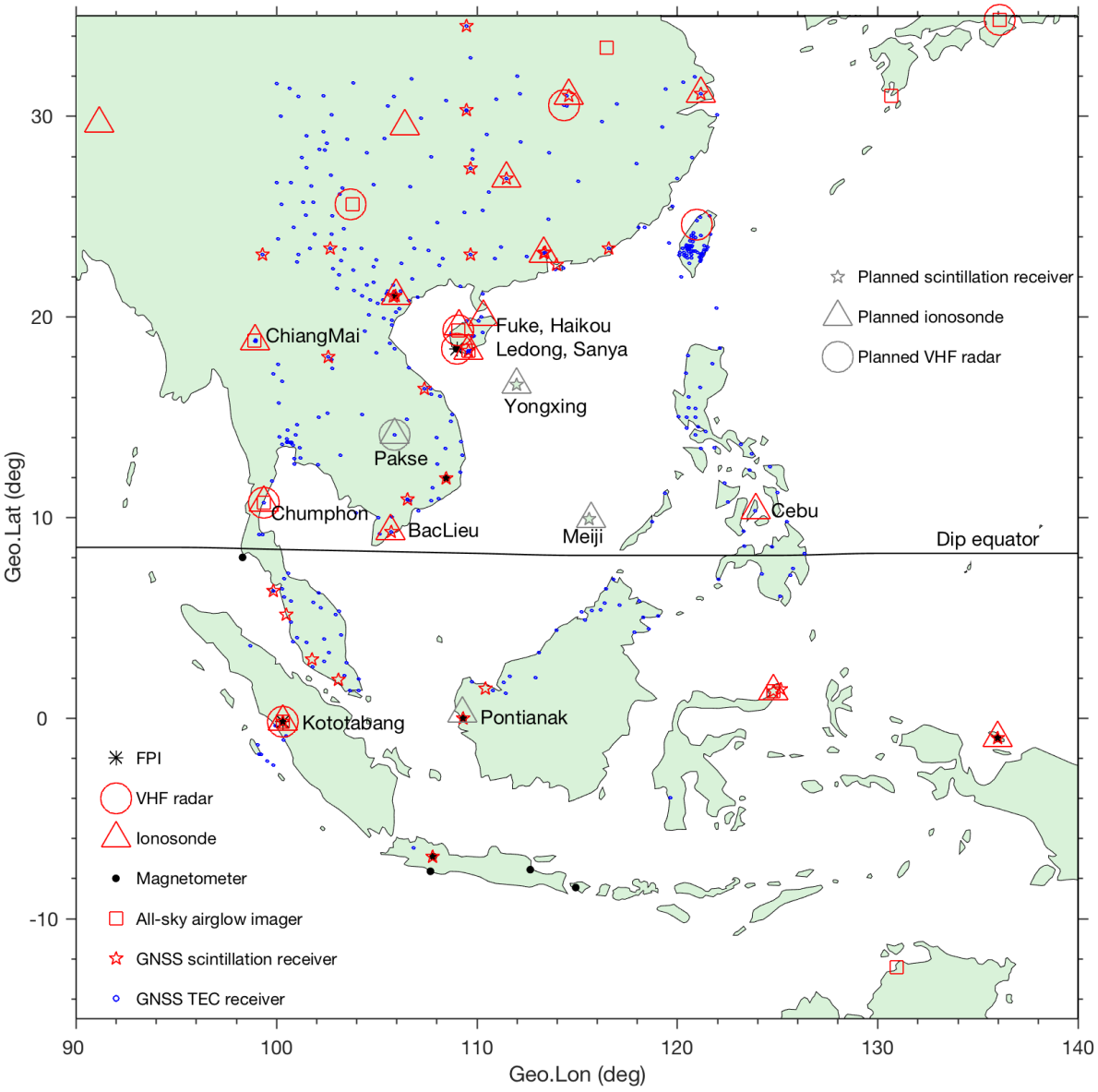

Figure 7. The geographical distributions of major ionospheric instruments that have been installed/planned for background ionosphere, EPB and its related irregularity and scintillation observations in the East and Southeast Asia. Part of station information are from previous publications, the Chinese Meridian Project network (https://data.meridianproject.ac.cn/), the IONISE network (http://ionise.geophys.ac.cn/index.asp), the SEALION network (http://seg-web.nict.go.jp/sealion/), and the Philippine Active Geodetic Network (PAGeNet) managed by National Mapping And Resource Information Authority (provided by Drs. Charisma Victoria De La Cruz Cayapan and Gabriella Povero).

5 Current observing capabilities for the ionosphere in East and Southeast Asia

A few observational networks and large facilities have been developed to study the ionosphere in the East and Southeast Asia, for example the SouthEast Asia Low-latitude Ionospheric Network (SEALION) (Maruyama et al., 2007), the Chinese Meridian Project (CMP) phase-I (Wang, 2010) and the Equatorial Ionosphere Characterization in Asia (ERICA) (Povero et al., 2017). These networks consist of various types of instruments including satellite beacon TEC/scintillation receiver, ionosonde, airglow imager and VHF radar. Some regional GNSS

receiver networks and all-sky airglow imager networks have been employed to monitor the ionosphere (e.g., Shiokawa et al., 1999; Otsuka et al., 2002; Aa et al., 2015; Sun et al., 2016; Buhari et al., 2017; Alfonsi et al., 2018). More recently, an ionospheric observation network for irregularity and scintillation in the East and Southeast Asia (INOISE), is being developed, which consists mainly of crossed chains of GNSS TEC/scintillation receivers, multi-static portable digital ionosondes (PDIs) and bistatic VHF coherent scatter radars (Li et al., 2019). Figure 7 shows the geographic distributions of some of these instruments for the observations of the background ionosphere, the EPBs and the related irregularity and scintillation distributions at equatorial and low latitudes. The grey symbols denote the instruments that are being planned.

5.1 Background ionosphere observation

As described above, the background ionosphere (including F layer height, F layer bottomside density wave structure, background ionospheric density, EIA, Es layer, and TIDs) and external driving forces (electric field and transequatorial wind) play important roles in the generation and evolution of EPB and its related irregularity and scintillation. In the East and Southeast Asia, three ionosondes operate at the stations Chumphon (10.7ºN, 99.4ºE), Baclieu (9.3ºN, 105.7ºE), and Cebu (10.4ºN,123.9ºE), which are close to the magnetic equator (Figure 7). These ionosondes transmit frequency-modulated continuous wave signals to sound the ionosphere and record ionograms at a temporal resolution of 5 min. Some ionospheric parameters can be estimated from the ionograms. For example the equatorial F layer height can be obtained through scaling the ionograms, and the equatorial vertical drift can be estimated from the temporal variation of F layer height ($\Delta h'F/\Delta t$). On the other hand, by measuring the difference in the magnitudes of the geomagnetic field horizontal component (ΔH) at magnetic equator and low latitudes (6-9° away from the magnetic equator), the vertical plasma drift at daytime can be derived using the established linear relationship between the vertical plasma drift and ΔH (Anderson et al., 2002). Some magnetometers have been deployed for long term observation of geomagnetic field at equatorial and low latitude sites (e.g., Yumoto, 2001).

The direct observation of F layer bottomside density wave structure can be obtained from steerable incoherent scatter radar (ISR). The wave structure preceding the generation of EPBs has been observed at both equatorial and low latitudes. At present, there is no steerable ISR operating at equatorial and low latitudes in the East and Southeast Asia. Under the support of National Natural Science Foundation of China (NSFC), a new ISR having the fast beam steering capability is under construction at low latitude Sanya. It is expected to start operation at the end of 2020. Whereas the earlier established techniques cannot directly measure the wave structure in this region, the ionosonde (e.g., Abdu et al., 1981b) and the GNU radio (a free software development framework) beacon receiver (Yamamoto, 2008) can be employed to measure ionogram 'satellite trace' and the longitudinal variation of TEC to characterize the presence of bottomside wave structure. Also, the periodic variations of F layer heights seen at different plasma frequencies are linked with bottomside wave structure (Abdu et al., 2015). Considering that the bottomside wave structure is necessary for the generation of EPBs, and the generation rate of EPBs is close to 100% under large upward vertical drifts, we infer that the bottomside wave structure could occur very often. The fast Doppler ionogram measurements by the multi-static PDIs (Lan et al., 2018) of IONISE will help understand the occurrence of bottomside density perturbation.

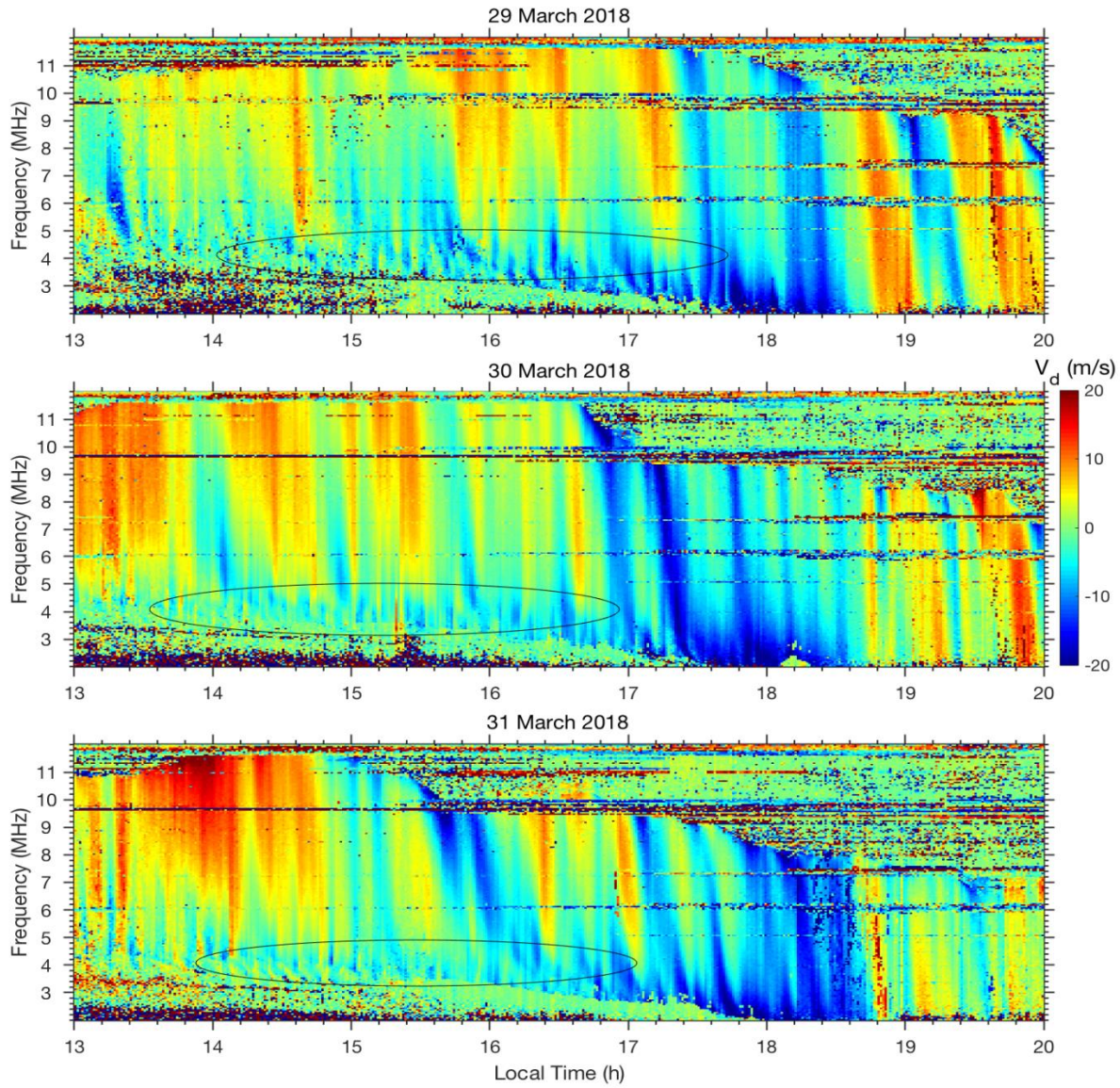

Figure 8. Ionospheric oscillations at different plasma frequencies derived from the fast Doppler ionograms recorded by the PDI at Sanya on 29-31 March 2018.

Figure 8 shows three cases of Doppler velocity oscillations measured at different plasma frequencies by the Sanya PDI on 29-31 March 2018. In the Doppler velocity maps (as functions of local time and plasma frequency), it can be seen that the velocity oscillations occur from afternoon to sunset hours on all the three days. The superimposed ellipses show the occurrence of F region bottomside perturbation with short periods during afternoon hours. Near sunset (17-19 LT), significant oscillation with relatively longer periods and larger amplitude was seen in the F region below the peak height. A preliminary analysis of the Doppler velocity maps from the Sanya PDI during March-April 2018 shows that these oscillations were observed almost every day (except several days without data due to the power failure). The future observations by multi-static PDIs with baselines of tens to hundreds of kilometers covering equatorial and low latitudes could provide the propagation characteristics of the waves that produce the F layer perturbations.

The observations of ionospheric electron density profile below the F layer topside, the EIA, Es layer, and TIDs can be well achieved with the regional GNSS TEC receiver networks and

numerous routine ionosondes. It is relevant to mention that the all-sky meteor radar, which is usually operated for specular meteor observation to derive neutral winds at 70-100 km, can be employed to simultaneously detect Es layer related irregularity structure over a large horizontal region and track its movement, without disrupting the meteor observation (Xie et al., 2019; Wang et al., 2019). The spatial morphology observation of Es structure by meteor radar will improve the understanding of E-F region coupling process. Regarding the thermospheric wind observation, one technique to measure this wind is by the use of Fabry-Perot interferometer (FPI), which can measure the atomic oxygen 630 nm red line emission to estimate the wind around 250 km altitude over a given site. There are two low latitude FPIs operating at Kototabang and Ledong (18.3ºN, 109ºE), which are in the opposite hemispheres. Another technique for determining the transequatorial thermospheric wind is to use magnetic conjugate ionosondes. The asymmetry of F layer height variation observed by the two ionosondes at magnetic conjugate stations Chiang Mai (18.8ºN, 98.9ºE) and Kototabang was suggested to be caused by transequatorial thermospheric wind along ~100ºE (Saito and Maruyama, 2006), which can suppress the generation of EPBs. Further, the magnetic conjugate ionosondes at Ledong and Pontianak (0.2ºN, 109.3ºE) can be employed to derive the transequatorial theremospheric wind along ~110°E. Based on these four ionosondes, the possible variation of transequatorial thermospheric winds and their effect on the generation of EPBs in a relatively small longitudinal region can be investigated.

5.2 EPB and its related irregularity and scintillation observation

Ionogram and TEC measurements have been extensively used to study the climatology of EPB occurrence since their first use several decades ago (e.g., Pi et al., 1997; Woodman, 2009; Shi et al., 2011; Alfonsi et al., 2013; Balan et al., 2018; the references therein). The range-type spread F (RSF) in the ionograms can be used to characterize irregularity structures with scale sizes ranging from several hundred kilometers to a few meters, the irregularity scale sizes decreasing through cascading process. It has been suggested that the RSF echoes at equatorial and low latitudes could originate primarily from the coherent backscatter mechanism (Abdu et al., 2012b). Due to the very wide beam width of ionosonde, the perpendicularity of ionosonde line-of-sight with the earth's magnetic field can be met within a large longitude and altitude range. The ionogram measurements over a chain of equatorial and low latitude stations in Brazil showed that the degree of range spreading of RSF echoes linearly increases with the top frequency of the echo trace, and that the irregularity strength exhibits a significant increase from the equator toward the EIA crests (similar to that of ionospheric scintillations) (Abdu et al., 2012b). It was suggested that the major characteristics of the RSF trace development are compatible with the process of coherent backscattering of the radio waves. The ionosondes widely distributed at equatorial and low latitudes in the East and Southeast Asia provide a good means for investigating the occurrence of different scale sizes EPB irregularities.

Using the dense regional TEC receiver networks in the East and Southeast Asia, the two-dimensional maps of the ROTI can be obtained to characterize the EPB occurrence. It is worth to mention that at solar minimum, the small ROTI values do not necessary represent the absence of EPBs due to the extremely low background density (Li et al., 2011). Based on a sequence of ROTI maps, the evolution of the horizontal structure of EPBs could be well investigated (e.g., Ma et al., 2006; Li et al., 2009a; Buhari et al., 2017; Aa et al., 2018). Unlike the widely distributed TEC receivers, the number of scintillation receivers in the East and Southeast Asia is limited, as marked by the pentacles in Figure 7. Another technique to get two-dimensional EPB map is by the use of all-sky airglow imager, which can obtain large-scale EPB depletion structure over a region as wide as ~2000 km in diameter including its variation with a good temporal resolution. From the measurements by dense TEC receiver

networks and all-sky airglow imagers, the zonal drift and spatial coverage of EPB and irregularity structure in both longitude and latitude can be derived. Due to the magnetic-field-aligned characteristics of EPBs, the horizontal structure of EPB can be mapped to the vertical plane over the magnetic equator.

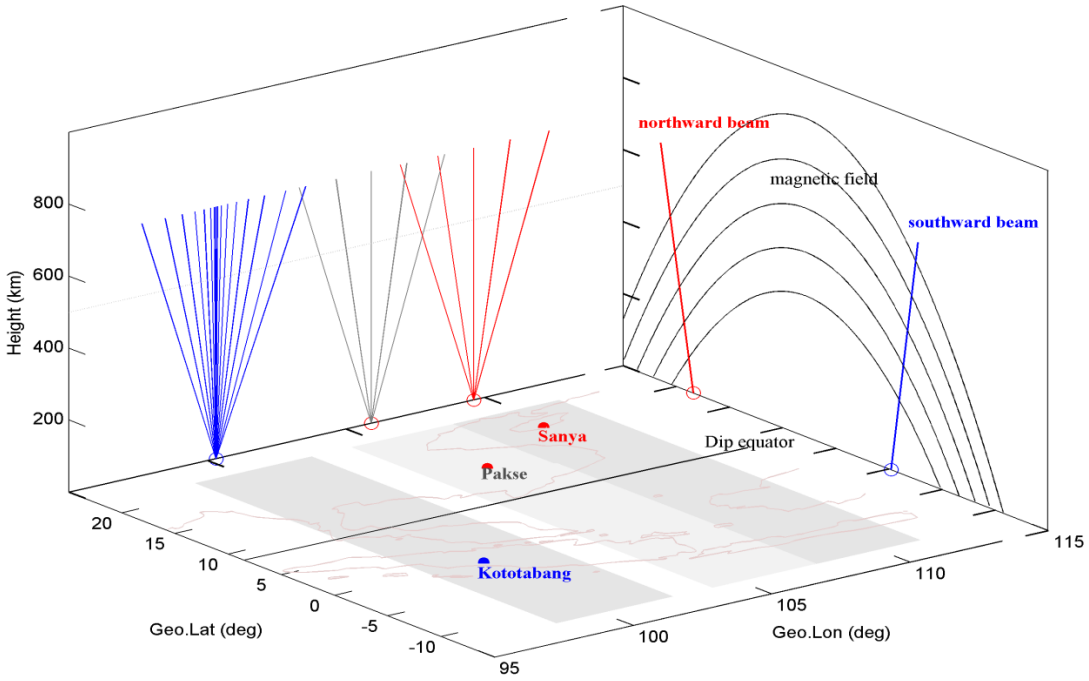

Figure 9. The field-of-views of the Kototabang, Pakse (planned) and Sanya VHF radars at 500 km altitude, covering almost the whole longitude region from ~100ºE to ~110ºE (updated from Li et al., 2016).

Steerable coherent backscatter radar measurements can provide information on the generation and evolution of EPB irregularity structure in the vertical-zonal plane. Some steerable VHF radars have been operated for a long time at low and middle latitudes in the East and Southeast Asia, for example at Kototabang, Sanya, Fuke (19.3ºN, 109.1ºE), Kunming (25.5ºN, 103.8ºE), Wuhan (30.5ºN, 114.3ºE), Shigaraki (34.9ºN, 136.1ºE), and Daejeon (36.2ºN, 127.1ºE) (e.g., Fukao et al., 1985, 2003; Otsuka et al., 2009; Wang et al., 2010; Ning et al., 2012; Li et al., 2018; Kwak et al., 2014; Zhou et al., 2018). Recently, a new VHF radar was set up at Chumphon by the National Institute of Information and Communications Technology, Japan. The Sanya VHF radar, which was relocated at Ledong in 2019, is being upgraded to a bistatic VHF radar system (with two reception sites separated by a few kilometers and synchronized by GPS pulse-per-second signal) that will provide high resolution imaging capability. The radar has a peak power of 72 kW and is expected to start operation in 2021. Another new VHF radar at Parkse (14.1ºN, 105.9ºE) is being planned. These radars, even though located at different latitudes/longitudes, can be employed together to track the occurrence and dynamics of EPBs in the Southeast Asia, and to reveal possible small-scale differences of EPB generation in longitude. Figure 9 shows an example of scanned areas by the Kototabang/Chumphon, Parkse and Ledong VHF radars. At an altitude of 500 km, the scanned area of each radar covers a region as wide as ~400 km or more in the east-west direction (as indicated by the horizontal shaded regions in Figure 9). The beam steering measurements provide a good spatial coverage and can well distinguish the EPBs generated locally in the shaded area from those drifting zonally. It is possible to track the whole process of EPB from its generation, spatial structural evolution, decay to disappearance over the longitude region of ~100ºE to ~110ºE.

6 Future developments in East and Southeast Asia

Despite that much progress has been made in the study of EPB and scintillation over the East and Southeast Asia, there are some gaps in our understanding of fundamental processes governing the day-to-day variability, due to lack of the information needed to discriminate among them. Through analyzing a large data series of scintillation and other parameters with machine learning algorithms, some efforts have been made in trying to improve the predictability of ionospheric scintillation (e.g., Rezende et al., 2010; Prikryl et al., 2013; de Lima et al., 2015). In general, when more parameters which affect the occurrence of EPB are included to train the sample, better forecast performance are achieved. Since there have been many years of observations of background ionosphere (for example the temporal variations of foF2 and hmF2) and of GPS scintillation at some low latitude stations in the East and Southeast Asia, it is possible to capture potential hidden and previously unknown information in the large databases with machine learning technique, and predict scintillation over the given site. On the other hand, by using numerical model simulation together with the feeding of measurements of various parameters, the day-to-day variability of the linear growth rate of R-T instability and the spatial/temporal variation of EPB were simulated (e.g., Carter et al., 2014; Wu, 2015; Sousasantos et al., 2017; Shinagawa et al., 2018). Through a comparison of simulated results with the observations of EPB/scintillation, it was found that a high R-T growth rate tends to correspond to the actual occurrence of EPB/scintillation. However, on a day-do-day basis, there are some discrepancies between the simulation and observation. To reliably forecast the temporal/spatial structure of EPB and strength of scintillation, an integrated model which is sensitive to ionosphere's day-to-day variability by incorporating atmospheric waves propagating from the lower atmosphere and polar energy inputs from the magnetosphere, is essential.

To better understand the day-to-day and short-term variability of EPBs in the East and Southeast Asia, the development of the observing capabilities to obtain the initial conditions (F region bottomside plasma density perturbation) and the driving forces on a regular basis is required. One is the expanded multi-static PDI network, which consists of five PDIs at Ledong, Meiji (9.9ºN, 115.7ºE), Yongxing (16.6ºN, 112.2ºE), Pakse (planned), and Pontianak (planned) for transmission and reception, and a lot of PDI receivers at different sites with baselines ranging from a few tens to more than one hundred kilometers around Hainan and Pakse. For each transmitting and receiving station, fast Doppler-ionograms (vertical/oblique) with a good temporal resolution (~1 min) can be obtained (Lan et al., 2018). Based on the multi-static PDI network, regional ionospheric profiles can be reconstructed. Besides TIDs, the F region bottomside plasma density perturbation structure in the east-west direction could be derived from the reconstruction results. Also, the equatorial F layer height and plasma vertical drift can be obtained from the PDI measurements at the magnetic equator station Meiji. The transequatorial wind information can be derived from the PDI measurements at the magnetic conjugate stations Ledong and Pontianak. These PDIs, together with the SEALION ionosondes at Cebu, BacLieu, Chumphon, Chiang Mai, and Kototabang may contribute to more accurate assessment of the local features of the driving forces. Meanwhile, if campaign experiments with the widely distributed instruments and regional networks are conducted in the East and Southeast Asia, the capability to observe the initial condition and driving forces for the EPB generation and evolution will be significantly enhanced.

Two large radar facilities have been planned at low latitude in the East and Southeast Asia. One is the equatorial middle and upper atmosphere (EMU) radar, which is planned to be deployed at Kototabang (Tsuda et al., 2016). This radar is designed with an operational

frequency of 47 MHz, a peak power of 500 kW and an antenna array consisting of 1045 Yagi antennas. The radar has the pulse-to-pulse beam steering capability for coherent and incoherent scatter observations. The other is the Hainan tristatic ISR facilities supported by the Chinese meridian project phase-II. The facilities consist of a UHF (~440 MHz) steerable radar (electronically formed beam) with a peak power of 4 MW and an array of 8192 antennas for transmission and reception at Sanya, and two steerable radars (each has 4096 antennas) for receptions at Fuke and Haikou (20ºN, 110.5ºE). As the most powerful instrument for observing the ionosphere, the steerable ISR can provide various parameters of ionosphere, for example, the F layer plasma vertical drift and electron density profiles over a wide region in the east-west direction, which are important for understanding the generation of the EPBs. The coordinated observations using the Hainan ISR facilities and Kototabang EMU radar may clarify unknown processes that cause some unusual phenomena in the longitudes and reveal the longitudinal variability of potential factors controlling the EPB generation.

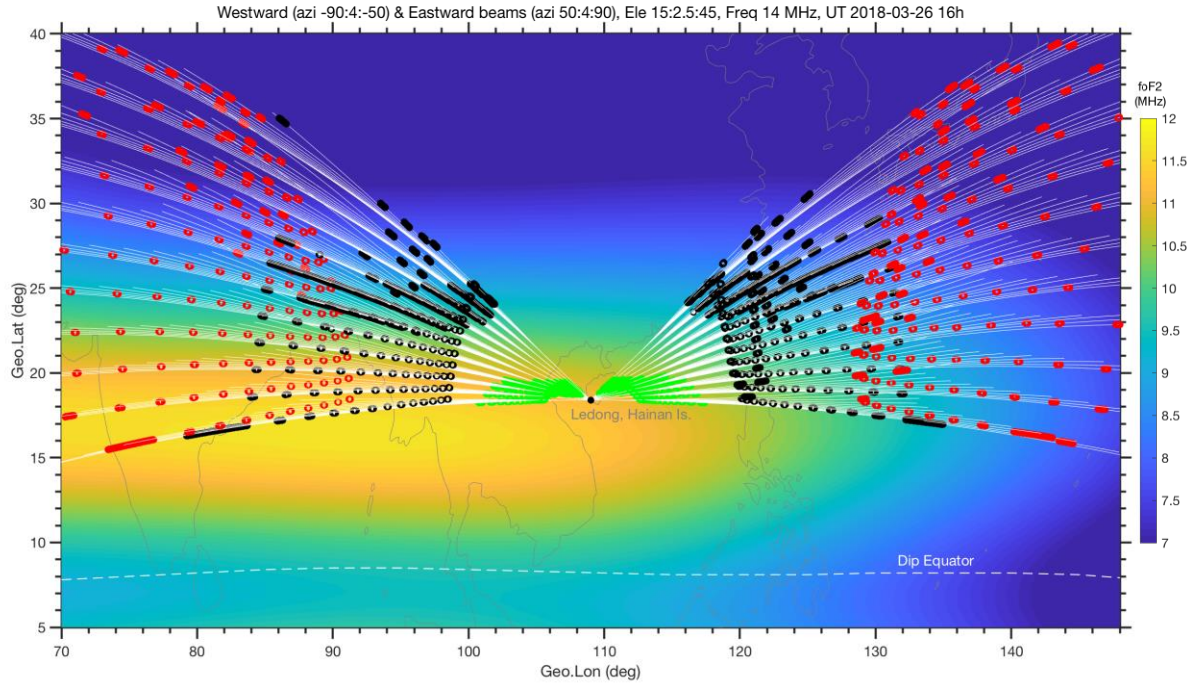

Figure 10. The modeled results for the westward and eastward beams of the Hainan HF coherent radar. The green (0.5 hop), black (1.5 hop) and red dots/circles (2.5 hop) represent the regions where the ray trace is perpendicular to geomagnetic field (within ±1º).

A new low latitude HF coherent radar, which is supported by the Chinese meridian project phase-II and aiming at detecting low latitude EPB irregularities, is being set up at Ledong. There have been some HF coherent radars at middle and high latitudes, which form the Super Dual Auroral Radar Network (SuperDARN) for observing ionospheric irregularity and the plasma dynamics (e.g., Nishitani et al., 2019). One main advantage of HF coherent radar is that it can receive backscatter echoes from a long horizontal distance of thousands of kilometers from the radar. Figure 10 shows the HF ray tracing simulation of the low latitude HF coherent radar at Ledong with the operational frequency 14 MHz. The HF ray path was calculated using the ray-tracing model developed by Jones and Stephenson (1975), together with the International Reference Ionosphere model (IRI-2012) (Bilitza et al., 2014) and the International Geomagnetic Reference Field model (IGRF-12) (Thébault et al., 2015). The color coding in the figure denotes the background ionospheric critical frequency estimated with the IRI model. The horizontal distributions of possible ionospheric backscatter echo regions, where the HF

radio wave vector is perpendicular to the geomagnetic field (within ±1°), are shown as green, black, and red dots/circles. The simulation results indicate that the HF coherent radar can detect irregularities appearing far away from the radar location, at 0.5-hop within ~1000 km (green), 1.5-hop within ~2500 km (black), and 2.5-hop within ~4000 km or more (red) in ground range. However, it is worth to point out that for the actual ionosphere which is very complicated due to various disturbances, it may be difficult to precisely determine the location of backscattered signals. We expect that this HF coherent radar, together with coordinated observations from the VHF radar, ionosonde and TEC receiver networks, provide important data for tracing the EPB irregularities over a wide longitudinal region and address the critical scientific problem, i.e., the day-to-day variability of EPBs over the East and Southeast Asia.

7 Conclusions

Great efforts have been made to establish regional dense observational networks and large facilities in the East and Southeast Asia. This enables an improved understanding on the generation and evolution of regional EPB and scintillations. We have presented a general review of the EPB and scintillation features, the physical mechanisms and controlling factors responsible for their occurrence, and unresolved issues related to their day-to-day and short-term variability. In general, the generation of EPB depends on (1) the F layer bottomside plasma density wave structure which initiates/seeds the R-T instability, and (2) the driving forces (background electric field and wind) which affect the F layer height and field-line-integrated conductivity and thus control the instability growth rate. During the upward growth of EPB from F region bottomside to topside over the magnetic equator, the large-scale polarization electric field generated within EPB can map to higher latitudes along magnetic field lines, causing similar large-scale structure of density depletion in both hemispheres. The peak altitude of EPB depends on the depletion depth and background density. Inside the depletion structure, plasma density irregularities of various scale sizes are generated locally through the cascading process, filling the depletion structure and causing severe scintillation of the radio waves traversing the EPB. The irregularity and resultant scintillation strengths, which depend on the background ionospheric density, are usually largest over the crest of equatorial ionization anomaly region.

In the East and Southeast Asia, the EPB and scintillation occur mainly during equinoctial months (March, April, September and October) when the driving force, the pre-reversal enhancement of eastward electric field (PRE), is strong. The PRE elevates the F layer to higher altitudes creating favorable conditions for the growth of R-T instability. The equinoctial EPBs are generated almost exclusively at post-sunset (for geomagnetic quiet condition) and sometimes continue into post-midnight hours. There is a good correspondence between the occurrences of the equinoctial EPB and the scintillation. At solar minimum, some EPBs are generated near midnight during June solstice, and preceded by substantial height rise of F layer. These solstitial post-midnight EPBs, ~~being~~ likely having ~~to have~~ a negative relationship with solar activity, do not cause ionospheric scintillation. The radar observations of solstitial post-midnight EPBs indicate that meter-scale irregularities were generated within the EPBs. The absence of scintillation may not be due to the absence of hundred meter-scale irregularities, but associated with the weak irregularity strength and extremely low background density. In general, the scintillation intensity is well correlated with EPB backscatter echo intensity. It is possible to determine the scintillation occurrence over a wide region based on radar multi-beam steering measurements.

The latitudinal extension of the EPBs is generally below ±25° (±18°) at 110°E under high (low) solar activity, corresponding to an apex altitude of 1050 km (550 km). The EPBs usually drift

eastward, with mean velocities ranging from 145 m/s to 75 m/s during 20-01 LT. The zonally drifting distance is estimated on average ~1250 km. During geomagnetic storms, the peak altitude and latitudinal extent of EPBs can be enhanced. Sometimes they rise to altitudes of 3400 km or more over the magnetic equator and map to middle latitudes of 40° or higher, producing super EPB and unusual scintillation events at middle latitudes. The eastward drifts of storm time EPBs can be weakened, and even reversed to westward under some conditions, with a latitudinal dependence in which the westward velocities increased with latitudes and west-tilted bubble structure was formed.

In longitude, EPBs are often generated periodically with separations of the order of a few hundreds to more than one thousand kilometers. Statistical studies have shown that there are extremely large differences in EPB generation rates at closely located longitudes (for example 54% and 28% over Kototabang and Sanya separated by ~1000 km, respectively). Considering that the driving forces, such as, the PRE, which control the growth of the R-T instability and often cover a large longitudinal region, the longitudinal difference could be linked with the local processes responsible for the F region bottomside seeding perturbation. The combined action of large-scale driving forces and relatively small scale local seeding determine whether or not EPB is generated and its day-to-day variability over a given longitude.

The relative importance of driving forces and local seeding on the day-to-day variability of EPB, however, is still not well known. The EPB generation is usually preceded by equatorial F layer height rise. This height rise, can be directly driven by the PRE and perturbation seeding source, i.e., gravity waves. Obvious difference of F layer height is observed at closely located longitudes. For the longitude with higher/lower F layer height, EPB is/not generated. It could be that the gravity waves modulate the F layer height, which being interrupted at higher altitudes with the start of EPB.

On the other hand, little is known on the day-to-day variability of the driving forces and local seeding, in itself. The PRE can be modified directly by the storm time electric field, and indirectly by gravity waves and planetary/Kelvin waves. The perturbation seeding, which is shown as large scale wave structure at F region bottomside, can be caused by the PRE related shear flow instability and gravity waves. Due to very limited measurements of the bottomside wave structure and the difficulty to directly detect gravity waves, it is unknown how the bottomside wave structure changes on a day-to-day basis. A preliminary analysis of Doppler ionogram during a two-month period shows that the F layer perturbations almost occur every day from afternoon to sunset hours over Sanya, which may indicate a high occurrence of the perturbation seeding. However, the thresholds of the bottomside wave structure parameters for EPB generation are not clear.

Whereas the general features of EPB and scintillation over the East and Southeast Asia are well known that enable the predictability of long-term variability, much remains to be done for reliably predicting their day-to-day and hourly variations. Ongoing efforts in the development of observing capability, including large radar facilities and regional dense TEC receiver, ionosonde oblique and vertical sounding networks, to better understand the initial perturbation and its seeding source in the East and Southeast Asia are needed. If the initial density perturbation over one given longitude can be obtained directly from observations, the short-term forecasting of locally generated EPBs may be developed by assimilating the EPB model and observation. For the EPBs generated elsewhere that may drift into the given longitude, the hourly forecasting can be achieved based on regional network observations.

Acknowledgments This work was supported by the National Natural Science Foundation of China (41727803, 41574149, 41422404, 41621063), the Hong Kong Research Grants Council (RGC) (No. B-Q61L PolyU 152222/17E), the JSPS KAKENHI Grant Number 15H05815 and 16H05736. The data used in this study are archived at the Geophysics Center, National Earth System Science Data Center at BNOSE, IGGCAS (http://wdc.geophys.ac.cn/). Authors are grateful to Charisma Victoria De La Cruz Cayapan (National Mapping And Resource Information Authority of the Republic of the Philippines) and Gabriella Povero (LINKS Foundation) for the station information of PAGeNet and IBISCO networks. During the peer review of this paper, the coauthor, very respected Professor Weixing Wan sadly passed away. We miss him dearly.

References

Aa, E., Huang, W., Liu, S. et al. (2015), A regional ionospheric TEC mapping technique over China and adjacent areas: GNSS data processing and DINEOF analysis. Sci. China Inf. Sci. 58, 1–11. https://doi.org/10.1007/s11432-015-5399-2.

Aa, E., Huang, W., Liu, S. et al. (2018), Midlatitude plasma bubbles over China and adjacent areas during a magnetic storm on 8 September 2017. Space Weather, 16, 321–331. https://doi.org/10.1002/2017SW001776.

Aarons, J. (1982), Global morphology of ionospheric scintillations, Proc. IEEE, 70, 360– 378, doi:10.1109/PROC.1982.12314.

Abadi, P., Saito, S., and Srigutomo, W. (2014), Low-latitude scintillation occurrences around the equatorial anomaly crest over Indonesia, Ann. Geophys., 32, 7–17, https://doi.org/10.5194/angeo-32-7-2014.

Abdu, M. A., J. A. Bittencourt, and I. S. Batista, (1981a), Magnetic declination control of the equatorial F region dynamo electric field development and spread F, J. Geophys. Res. 86, A13, 11,443-11,446.

Abdu, M. A., I. S. Batista, and J. A. Bittencourt (1981b), Some characteristics of spread F at the magnetic equatorial station Fortaleza, J. Geophys. Res., 86 (A8), 6836–6842.

Abdu, M. A., R. T. de Meiros, J. H. A. Sobrel, and J. A. Bittencourt (1983), Spread F plasma bubble vertical rise velocities determined from spaced ionosonde observations, J. Geophys. Res., 88, 9197– 9204.

Abdu, M. A. (2001). Outstanding problems in the equatorial ionosphere thermosphere electrodynamics relevant to spread F. Journal of Atmospheric and Solar-Terrestrial Physics, 63(9), 869–884.

Abdu, M.A. et al. (2008), Abnormal evening vertical plasma drift and effects on ESF and EIA over Brazil-South Atlantic sector during the 30 October 2003 superstorm. J Geophys Res 113: A07313. https://doi.org/10.1029/2007JA012844.

Abdu, M. A., I. S. Batista, B. W. Reinisch, et al. (2009), Conjugate Point Equatorial Experiment (COPEX) campaign in Brazil: Electrodynamics highlights on spread F development conditions and day-to-day variability, J. Geophys. Res., 114, A04308, doi:10.1029/2008JA013749.

Abdu, M. A. (2012), Equatorial spread F/plasma bubble irregularities under storm time disturbance electric fields. Journal of Atmospheric and Solar-Terrestrial Physics, 75-76, 44–56. https://doi.org/10.1016/j.jastp.2011.04.024.

Abdu, M. A., I. S. Batista, B. W. Reinisch, et al. (2012), Equatorial range spread F echoes from coherent backscatter, and irregularity growth processes, from conjugate point digital ionograms, Radio Sci., 47, RS6003, doi:10.1029/2012RS005002.

Abdu, M. A., de Souza JR, Kherani EA, et al. (2015a), Wave structure and polarization electric field development in the bottomside F layer leading to postsunset equatorial spread F. J Geophys Res 120:6930. https://doi.org/10.1002/2015JA021235.

Abdu, M. A., Brum, C. G. M, Batista, P. P., et al. (2015b), Fast and ultrafast Kelvin wave modulations of the equatorial evening F region vertical drift and spread F development. Earth Planets Space 67:1. https://doi.org/10.1186/s40623-014-0143-5.

Abdu, M. A. (2019), Day-to-day and short-term variabilities in the equatorial plasma bubble/spread F irregularity seeding and development. Prog Earth Planet Sci, 6, 11. https://doi.org/10.1186/s40645-019-0258-1.

Ajith, K. K., Tulasi Ram, S., Carter, B.A. et al. (2018), Unseasonal development of post-sunset F-region irregularities over Southeast Asia on 28 July 2014: 2. Forcing from below?. Prog Earth Planet Sci 5, 60. https://doi.org/10.1186/s40645-018-0218-1.

Alfonsi, L., Spogli, L., Tong, J. R., et al. (2011), GPS scintillation and TEC gradients at equatorial latitudes in April 2006. Advances in space Research, 47(10), 1750-1757.

1211 Alfonsi, L., Spogli, L., Pezzopane, et al. (2013), Comparative analysis of spread-F signature and GPS scintillation
1212 occurrences at Tucumán, Argentina, J. Geophys. Res. Space Physics, 118, 4483– 4502, doi:10.1002/jgra.50378.
1213 Alfonsi, L., Wernik, A. W., Materassi, M., & Spogli, L. (2017), Modelling ionospheric scintillation under the
1214 crest of the equatorial anomaly. Advances in Space Research, 60(8), 1698-1707.
1215 Alfonsi, L., et al. (2018), Analysis of the regional ionosphere at low latitudes in support of the biomass ESA
1216 mission, IEEE transactions on Geoscience and remote sensing, 56, 11, 6412-6422.
1217 Anderson, D., Anghel, A., Yumoto, et al. (2002), Estimating daytime vertical ExB drift velocities in the equatorial
1218 F-region using ground-based magnetometer observations, Geophys. Res. Lett., 29 (12),
1219 doi:10.1029/2001GL014562.
1220 Balan, N., Maruyama, T., Patra, A. K. et al. (2018), A minimum in the latitude variation of spread-F at March
1221 equinox. Prog Earth Planet Sci 5, 27. https://doi.org/10.1186/s40645-018-0180-y.
1222 Basu, S., and S. Basu (1981), Equatorial scintillations- A review, J. Atmos. Terr. Phys., 43, 473-489.
1223 Basu, S., Mackenzie, E., Basu, S., (1988), Ionospheric constraints on VHF/UHF communication links during solar
1224 maximum and minimum periods. Radio Science 23, 363-372.
1225 Bilitza, D., D. Altadill, Y. Zhang, et al. (2014), The International Reference Ionosphere 2012 -a model of
1226 international collaboration, J. Space Weather Space Clim., 4 (A07), https://doi.org/10.1051/swsc/2014004.
1227 Bhattacharyya, A. (1990), Chaotic behaviour of ionospheric turbulence from scintillation measurements, Geophys.
1228 Res. Lett., https://doi.org/10.1029/GL017i006p00733.
1229 Bhattacharyya, A., S. Basu, K. M. Groves, et al. (2001), Dynamics of equatorial F region irregularities from
1230 spaced receiver scintillation observations, Geophys. Res. Lett., 28(1), 119–122.
1231 Buhari, S. M., Abdullah, M., Yokoyama, et al. (2017), Climatology of successive equatorial plasma bubbles
1232 observed by GPS ROTI over Malaysia, J. Geophys. Res. Space Physics, 122, 2174-
1233 2184, doi:10.1002/2016JA023202.
1234 Carrasco, A., Batista, I., and Abdu, M. (2005). The pre reversal enhancement in the vertical drift for Fortaleza and
1235 the sporadic E layer, Journal of Atmospheric and Solar-Terrestrial
1236 Physics, 67(16), 1610– 1617, https://doi.org/10.1016/j.jastp.2005.07.015.
1237 Carter B.A., et al. (2014) Geomagnetic control of equatorial plasma bubble activity modeled by the TIEGCM
1238 with Kp, Geophys Res Lett, 41:5331-5339. https://doi.org/10.1002/ 2014GL060953.
1239 Carter, B., Ram, S., Yizengaw, E. et al. (2018), Unseasonal development of post-sunset F-region irregularities
1240 over Southeast Asia on 28 July 2014: 1. Forcing from above?. Prog Earth Planet Sci 5, 10.
1241 https://doi.org/10.1186/s40645-018-0164-y.
1242 Cervera, M.A., Thomas, R.M., Groves, K.M., et al. (2001), Validation of WBMOD in the Southeast Asian region.
1243 Radio Sci., 36:1559–1572.
1244 Cesaroni, C., Spogli, L., Alfonsi, L., et al. (2015), L-band scintillations and calibrated total electron content
1245 gradients over Brazil during the last solar maximum. Journal of Space Weather and Space Climate, 5, A36.
1246 Chau, J. L., Woodman, R. F., (2001), Interferometric and dual beam observations of daytime spread-F-like
1247 irregularities over Jicamarca. Geophys Res Lett 28(18): 3581–3584.
1248 Chen, G. et al. (2017), Low-latitude daytime F region irregularities observed in two geomagnetic quiet days by
1249 the Hainan coherent scatter phased array radar (HCOPAR). J Geophys Res Space Physics 122:2645–2654.
1250 https://doi.org/10.1002/2016JA023628.
1251 Costa, E., E. R. de Paula, L. F. C. Rezende, et al. (2011), Equatorial scintillation calculations based on coherent
1252 scatter radar and C/NOFS data, Radio Sci., 46, RS2011, doi:10.1029/2010RS004435.
1253 Dao, E., M. C. Kelley, D. L. Hysell, et al. (2012), On the distribution of ion density depletion along magnetic field
1254 lines as deduced using C/NOFS, Radio Sci., 47, RS3001, doi:10.1029/2011RS004967.
1255 Dao, T, Otsuka Y, Shiokawa K, et al. (2017) Coordinated observations of postmidnight irregularities and
1256 thermospheric neutral winds and temperatures at low latitudes. J Geophys Res Space Physics 122.
1257 https://doi.org/10.1002/2017JA024048.
1258 de Lima, G. R, T., Stephany, S., de Paula, E. R., et al. (2015), Prediction of the level of ionospheric scintillation
1259 at equatorial latitudes in Brazil using a neural network. Space Weather, 13(8): 446-457.
1260 Eccles, J. V., St Maurice, J. P., Schunk, R. W. (2015) Mechanisms underlying the prereversal enhancement of the
1261 vertical plasma drift in the low-latitude ionosphere. J Geophys Res Space Physics 120:4950–4970.
1262 https://doi.org/10.1002/2014JA020664.
1263 Fejer, B.G., Scherliess, L., dePaula, E.R. (1999), Effects of the vertical plasma drift velocity on the generation
1264 and evolution of equatorial spread F. J Geophys Res 104(A9):19859–19869.

Fejer, B. G., J. de Souza, A. S. Santos, and A. E. Costa Pereira (2005), Climatology of F region zonal plasma drifts over Jicamarca, J. Geophys. Res., 110, A12310, doi:10.1029/2005JA011324.

Fritts, D.C. et al. (2008), Gravity wave and tidal influences on equatorial spread F based on observations during the Spread F Experiment (SpreadFEx). Ann Geophys 26:3235–3252, http://www.ann-geophys.net/26/3235/2008/.

Fukao, S., Tsuda, T., Sato, T., et al. (1985), The MU radar with an active phased array system: 2. In-house equipment, Radio Sci., 20(6), 1169–1176, doi:10.1029/RS020i006p01169.

Fukao, S., Y. Ozawa, M. Yamamoto, and R. T. Tsunoda (2003), Altitude extended equatorial spread F observed near sunrise terminator over Indonesia, Geophys. Res. Lett., 30(22), 2137, doi:10.1029/2003GL018383.

Grzesiak, M., Cesaroni, C., Spogli, L., De Franceschi, G., and Romano, V. (2018), Regional short-term forecasting of ionospheric TEC and scintillation. Radio Science, 53(10), 1254-1268.

Haerendel, G. (1974), Theory of Equatorial Spread F, Max-Planck Inst. für Extraterr. Phys., Munich, Germany.

Hu L., Ning B., Li G., and Li M. (2014). Observations on the field-aligned irregularities using Sanya VHF radar: 4. June solstitial F-region echoes in solar minimum. Chinese J. Geophys. (in Chinese), 57(1): 1-9, doi: 10.6038/cjg20140101.

Huang, C.-S., O. de La Beaujardiere, R. F. Pfaff, et al. (2010), Zonal drift of plasma particles inside equatorial plasma bubbles and its relation to the zonal drift of the bubble structure, J. Geophys. Res., 115, A07316, doi:10.1029/2010JA015324.

Huang, C.-S., O. de La Beaujardiere, P. A. Roddy, et al. (2012), Generation and characteristics of equatorial plasma bubbles detected by the C/NOFS satellite near the sunset terminator, J. Geophys. Res., 117, A11313, doi:10.1029/2012JA018163.

Huang, C.-S., de La Beaujardiere, O., Roddy, P. A., et al. (2014), Occurrence probability and amplitude of equatorial ionospheric irregularities associated with plasma bubbles during low and moderate solar activities (2008–2012), J. Geophys. Res. Space Physics, 119, 1186– 1199, doi:10.1002/2013JA019212.

Huang, C., and Hairston, M. R. (2015), The postsunset vertical plasma drift and its effects on the generation of equatorial plasma bubbles observed by the C/NOFS satellite. J. Geophys. Res. Space Physics, 120, 2263– 2275. doi: 10.1002/2014JA020735.

Huang, C.-S., and P. A. Roddy (2016), Effects of solar and geomagnetic activities on the zonal drift of equatorial plasma bubbles, J. Geophys. Res. Space Physics, 121, 628–637, doi:10.1002/2015JA021900.

Huang, C.-S. (2018), Effects of the postsunset vertical plasma drift on the generation of equatorial spread F. Prog Earth Planet Sci 5, 3. https://doi.org/10.1186/s40645-017-0155-4.

Hysell DL, Kudeki E (2004), Collisional shear instability in the equatorial F region ionosphere. J Geophys Res 109: A11301. https://doi.org/10.1029/2004JA010636.

Jones, R.M. and Stephenson, J. J. (1975), A versatile three-dimensional ray tracing computer program for radio waves in the ionosphere, U.S. Department of Commerce, OT Report 1/10.

Joshi, L. M., A. K. Patra, T. K. Pant, and S. V. B. Rao (2013), On the nature of low-latitude Es influencing the genesis of equatorial plasma bubble, J. Geophys. Res. Space Physics, 118, 524–532, doi:10.1029/2012JA018122.

Joshi, L. M., S. Balwada, T. K. Pant, and S. G. Sumod (2015), Investigation on F layer height rise and equatorial spread F onset time: Signature of standing large-scale wave, Space Weather, 13, 211–219, doi:10.1002/2014SW001129.

Katamzi-Joseph, Z. T., Habarulema, J. B., & Hernández-Pajares, M. (2017). Midlatitude postsunset plasma bubbles observed over Europe during intense storms in April 2000 and 2001. Space Weather, 15, 1177–1190. https://doi.org/10.1002/2017SW001674

Kelley, M. C. (2009). The Earth's ionosphere: Plasma physics and electrodynamics, Int. Geophys. Ser. (Vol. 43). San Diego, CA: Academic Press.

Kelly, M. A., Comberiate, J. M., Miller, E. S., and Paxton, L. J. (2014), Progress toward forecasting of space weather effects on UHF SATCOM after Operation Anaconda, Space Weather, 12, 601– 611, doi:10.1002/2014SW001081.

Kil, H., Paxton, L. J., Oh S-J (2009), Global bubble distribution seen from ROCSAT-1 and its association with the evening prereversal enhancement. J Geophys Res 114:A06307. https://doi.org/10.1029/2008JA013672.

Kil, H., Paxton, L. J., Lee, W. K., & Jee, G. (2019). Daytime evolution of equatorial plasma bubbles observed by the first Republic of China satellite. Geophysical Research Letters, 46, 5021–5027. https://doi.org/10.1029/2019GL082903.

Kintner, P.M., Kil, H., Beach, T.L., and de Paula, E.R. (2001), Fading timescales associated with GPS signals and potential consequences, Radio Science, 36 (4), 731-743.

Krall, J., Huba, J. D., Ossakow, S. L., and Joyce, G. (2010), Why do equatorial ionospheric bubbles stop rising? *Geophys. Res. Lett.*, 37, L09105, doi:10.1029/2010GL043128.

Krall, J., J. D. Huba, S. L. Ossakow, et al. (2011), Modeling of equatorial plasma bubbles triggered by nonequatorial traveling ionospheric disturbances, Geophys. Res. Lett., 38, L08103, doi:10.1029/2011GL046890.

Kwak, Y., Yang T., Kil H., et al. (2014), Characteristics of the E- and F-region field-aligned irregularities in middle latitudes: Initial results obtained from the Daejeon 40.8 MHz VHF radar in South Korea, J. Astron. Space Sci. 31(1), 15-23.

LaBelle, J. (1985), Mapping of electric field structures from the equatorial F region to the underlying E region, J. Geophys. Res., 90, 4341–4346, doi:10.1029/JA090iA05p04341.

Lan, J., Ning, B., Li, G., et al. (2018). Observation of short-period ionospheric disturbances using a portable digital ionosonde at Sanya. Radio Science, 53, 1521–1532. https://doi.org/10.1029/2018RS006699.

Liang, B.-X., Li, J., and Ma, S.-Y. (1994), Progress of Ionospheric Research in China, Chinese Journal of Geophysics, 37(S1): 51-73.

Li G, Ning B, Liu L, et al. (2007), The correlation of longitudinal/ seasonal variations of evening equatorial pre-reversal drift and of plasma bubbles. Ann Geophys 25:2571–2578.

Li, G., Ning, B., Zhao, B., et al. (2009a). Characterizing the 10 November 2004 storm-time middle-latitude plasma bubble event in Southeast Asia using multi-instrument observations. Journal of Geophysical Research, 114, A07304. https://doi.org/10.1029/2009JA014057.

Li, G., B. Ning, L. Liu, W. Wan, and J.Y. Liu (2009b), Effect of magnetic activity on plasma bubbles over equatorial and low-latitude regions in East Asia, Annales Geophysicae, 27, 303-312.

Li, G., et al. (2010), Longitudinal development of low-latitude ionospheric irregularities during the geomagnetic storms of July 2004, J. Geophys. Res., 115, A04304, doi:10.1029/2009JA014830.

Li, G., B. Ning, M. A. Abdu, et al. (2011), On the occurrence of postmidnight equatorial F region irregularities during the June solstice, J. Geophys. Res., 116, A04318, doi:10.1029/2010JA016056.

Li, G., B. Ning, M. A. Abdu, W. Wan, and L. Hu (2012), Precursor signatures and evolution of post-sunset equatorial spread-F observed over Sanya, J. Geophys. Res., 117, A08321, doi:10.1029/2012JA017820.

Li, G., Ning, B., Abdu, M. A., et al. (2013). Longitudinal characteristics of spread F backscatter plumes observed with the EAR and Sanya VHF radar in Southeast Asia. Journal of Geophysical Research: Space Physics, 118, 6544–6557. https://doi.org/10.1002/jgra.50581.

Li, G., Y. Otsuka, B. Ning, et al. (2016), Enhanced ionospheric plasma bubble generation in more active ITCZ, Geophys. Res. Lett., 43, 2389–2395, doi:10.1002/2016GL068145.

Li, G., Ning, B., Wang, C., et al. (2018a). Storm-enhanced development of postsunset equatorial plasma bubbles around the meridian 120°E/60°W on 7–8 September 2017. Journal of Geophysical Research: Space Physics, 123, 7985–7998. https://doi.org/10.1029/2018JA025871.

Li, G., Ning, B., Abdu, M.A. et al. (2018b), Daytime F-region irregularity triggered by rocket-induced ionospheric hole over low latitude. Prog Earth Planet Sci, 5, 11. https://doi.org/10.1186/s40645-018-0172-y.

Li, G., Ning, B., Zhao, X., et al. (2019). Low latitude ionospheric TEC oscillations associated with periodic changes in IMF Bz polarity. Geophysical Research Letters, 46. https://doi.org/10.1029/2019GL084428.

Liu, K., Li, G., and Ning, B. (2019), Possible evidence for small-scale wave seeding of equatorial plasma bubbles, Advances in Space Research, 11, 63, 3612-3620, https://doi.org/10.1016/j.asr.2019.02.025.

Liu, K., Li, G., Ning, B., Hu, L., Li, H. (2015), Statistical characteristics of low-latitude ionospheric scintillation over China, Advances in Space Research, 55(5):1356-1365, doi:10.1016/j.asr.2014.12.001.

Ma, G., & Maruyama, T. (2006). A super bubble detected by dense GPS network at east Asian longitudes. Geophysical Research Letters, 33, L21103. https://doi.org/10.1029/2006GL027512.

Maruyama, T. (1988), A diagnostic model for equatorial spread F, 1, Model description and application to electric field and neutral wind effects, J. Geophys. Res., 93(A12), 14611– 14622, doi:10.1029/JA093iA12p14611.

Maruyama, T. and Kawamura, M. (2006), Equatorial ionospheric disturbance observed through a transequatorial HF propagation experiment, Ann. Geophys., 24, 1401–1409, https://doi.org/10.5194/angeo-24-1401-2006.

Maruyama, T., Kawamura, M., Saito, S., et al. (2007), Low latitude ionosphere-thermosphere dynamics studies with ionosonde chain in Southeast Asia, Ann. Geophys., 25, 1569–1577, https://doi.org/10.5194/angeo-25-1569-2007.

Maruyama, T., Saito S, Kawamura, M., et al. (2009), Equinoctial asymmetry of a low-latitude ionosphere-thermosphere system and equatorial irregularities: evidence for meridional wind control. Ann Geophys, 27:2027.

McClure, J. P., S. Singh, D. K. Bamgboye, et al. (1998), Occurrence of equatorial F region irregularities: Evidence

for tropospheric seeding, J. Geophys. Res., 103, 29,119-29,135.

Mendillo, M., E. Zesta, S. Shodham, et al. (2005), Observations and modeling of the coupled latitude-altitude patterns of equatorial plasma depletions, *J. Geophys. Res.*, 110, A09303, doi:10.1029/2005JA011157.

Mohanty, S., Singh, G., Carrano, C. S., & Sripathi, S. (2018). Ionospheric scintillation observation using space-borne synthetic aperture radar data. Radio Science, 53, 1187– 1202. https://doi.org/10.1029/2017RS006424.

Muella, M. T. A. H., Duarte-Silva, M. H., Moraes, A. O., et al. (2017), Climatology and modeling of ionospheric scintillations and irregularity zonal drifts at the equatorial anomaly crest region, Ann. Geophys., 35, 1201–1218, https://doi.org/10.5194/angeo-35-1201-2017.

Ning, B., Hu, L., Li, G., et al. (2012), The first time observations of low-latitude ionospheric irregularities by VHF radar in Hainan. Sci China Tech Sci, doi: 10.1007/s11431-012-4800-2.

Nishioka, M., Otsuka, Y., Shiokawa, K., et al. (2012), On post-midnight field-aligned irregularities observed with a 30.8-MHz radar at a low latitude: comparison with F-layer altitude near the geomagnetic equator. J Geophys Res 117: A08337. https://doi.org/10.1029/2012JA017692.

Nishitani, N., Ruohoniemi, J.M., Lester, M. et al. (2019), Review of the accomplishments of mid-latitude Super Dual Auroral Radar Network (SuperDARN) HF radars. Prog Earth Planet Sci 6, 27. https://doi.org/10.1186/s40645-019-0270-5.

Otsuka, Y., Shiokawa, K., Ogawa, T., and Wilkinson, P. (2002a), Geomagnetic conjugate observations of equatorial airglow depletions, Geophys. Res. Lett., 29 (15), doi:10.1029/2002GL015347.

Otsuka, Y., Ogawa, T., Saito, A., et al., (2002b), A new technique for mapping of total electron content using GPS network in Japan, Earth Planets Space, 54, 63–70.

Otsuka, Y., Shiokawa, K., and Ogawa, T. (2006), Equatorial Ionospheric Scintillations and Zonal Irregularity Drifts Observed with Closely-Spaced GPS Receivers in Indonesia, Journal of the Meteorological Society of Japan, 84A, 343-351, 2006.

Otsuka, Y., Ogawa, T., Effendy (2009), VHF radar observations of nighttime F-region field-aligned irregularities over Kototabang, Indonesia. Earth Planets Space 61(4):431–437.

Otsuka, Y. (2018), Review of the generation mechanisms of post-midnight irregularities in the equatorial and low-latitude ionosphere. Prog Earth Planet Sci 5, 57. https://doi.org/10.1186/s40645-018-0212-7.

Patra, A. K., D. V. Phanikumar, and T. K. Pant (2009), Gadanki radar observations of F region field-aligned irregularities during June solstice of solar minimum: First results and preliminary analysis, J. Geophys. Res., 114, A12305, doi:10.1029/2009JA014437.

Patra, A. K., Taori, A., Chaitanya, P. P., and Sripathi, S. (2013), Direct detection of wavelike spatial structure at the bottom of the F region and its role on the formation of equatorial plasma bubble, J. Geophys. Res. Space Physics, 118, 1196–1202, doi:10.1002/jgra.50148.

Pi, X., A. J. Mannucci, U. J. Lindqwister, and C. M. Ho (1997), Monitoring of global ionospheric irregularities using the worldwide GPS network, Geophys. Res. Lett., 24, 2283– 2286, doi:10.1029/97GL02273.

Povero, G., et al. (2017), Ionosphere Monitoring in South East Asia in the ERICA Study, NAVIGATION: Journal of The Institute of Navigation, 0, 0.

Prikryl, P., Sreeja, V., Aquino, M., and Jayachandran, P. T. (2013), Probabilistic forecasting of ionospheric scintillation and GNSS receiver signal tracking performance at high latitudes, Annals of Geophysics, 56, 2, R0222, doi:10.4401/ag-6219.

Rezende, L. F. C., de Paula, E. R., Stephany, S., et al. (2010), Survey and prediction of the ionospheric scintillation using data mining techniques, Space Weather, 8, S06D09, doi:10.1029/2009SW000532.

Rodrigues, F., Hickey, D., Zhan, W. et al. (2018), Multi-instrumented observations of the equatorial F-region during June solstice: large-scale wave structures and spread-F. Prog Earth Planet Sci 5, 14. https://doi.org/10.1186/s40645-018-0170-0.

Sahai, Y., et al. (2009), Effects observed in the ionospheric F region in the east Asian sector during the intense geomagnetic disturbances in the early part of November 2004, J. Geophys. Res., 114, A00A18, doi:10.1029/2008JA013053.

Saito, S. and Maruyama, T. (2006), Ionospheric height variations observed by ionosondes along magnetic meridian and plasma bubble onsets, Ann. Geophys., 24, 2991–2996, https://doi.org/10.5194/angeo-24-2991-2006.

Saito, S., and T. Maruyama (2007), Large-scale longitudinal variation in ionospheric height and equatorial spread F occurrences observed by ionosondes, Geophys. Res. Lett., 34, L16109, doi:10.1029/ 2007GL030618.

Seo, J., Walter, T., Chiou, T.-Y., and Enge, P. (2009), Characteristics of deep GPS signal fading due to ionospheric scintillation for aviation receiver design, Radio Sci., 44, RS0A16, doi:10.1029/2008RS004077.

Shi, J. K., Wang, G. J., Reinisch, B. W., et al. (2011), Relationship between strong range spread F and ionospheric scintillations observed in Hainan from 2003 to 2007, J. Geophys. Res., 116, A08306, doi:10.1029/2011JA016806.

Shinagawa, H., Jin, H., Miyoshi, Y. et al. (2018), Daily and seasonal variations in the linear growth rate of the Rayleigh-Taylor instability in the ionosphere obtained with GAIA. Prog Earth Planet Sci 5, 16. https://doi.org/10.1186/s40645-018-0175-8.

Shiokawa, K., Katoh, Y., Satoh, M., et al. (1999), Development of Optical Mesosphere Thermosphere Imagers (OMTI), Earth Planets Space, 51, 887–896.

Shiokawa, K., Otsuka, Y., Ogawa, T., and Wilkinson, P. (2004), Time evolution of high-altitude plasma bubbles imaged at geomagnetic conjugate points, Ann. Geophys., 22, 3137–3143, https://doi.org/10.5194/angeo-22-3137-2004.

Smith, J., and Heelis, R. A. (2017), Equatorial plasma bubbles: Variations of occurrence and spatial scale in local time, longitude, season, and solar activity, J. Geophys. Res. Space Physics, 122, 5743– 5755, doi:10.1002/2017JA024128.

Sousasantos, J., E. A. Kherani, and J. H. A. Sobral (2017), An alternative possibility to equatorial plasma bubble forecasting through mathematical modeling and Digisonde data, J. Geophys. Res. Space Physics, 122, 2079–2088, doi:10.1002/2016JA023241.

Spogli, L., et al. (2016), Formation of ionospheric irregularities over Southeast Asia during the 2015 St. Patrick's Day storm, J. Geophys. Res. Space Physics, 121, 12,211– 12,233, doi:10.1002/2016JA023222.

Su, S. Y., Liu, C. H., Ho, H. H., Chao, C. K. (2006), Distribution characteristics of density irregularities: equatorial versus midlatitude regions, J Geophys Res., 111: A06305. doi: 10.1029/2005JA011330 A06305.

Sultan, P. J. (1996), Linear theory and modeling of the Rayleigh-Taylor instability leading to the occurrence of equatorial spread F, J. Geophys. Res., 101 (A12), 26875– 26891, doi:10.1029/96JA00682.

Sun, L., Xu, J., Wang, W., et al. (2016), A statistical analysis of equatorial plasma bubble structures based on an all-sky airglow imager network in China, J. Geophys. Res. Space Physics, 121, 11,495– 11,517, doi:10.1002/2016JA022950.

Takahashi, H., et a. (2009), Simultaneous observation of ionospheric plasma bubbles and mesospheric gravity waves during the SpreadFEx Campaign, Ann. Geophys., 27, 1477–1487, https://doi.org/10.5194/angeo-27-1477-2009.

Takahashi, H., et al. (2010), Equatorial ionosphere bottom-type spread F observed by OI 630.0 nm airglow imaging, Geophys. Res. Lett., 37, L03102, doi:10.1029/2009GL041802.

Takahashi, H., et al (2018). Equatorial plasma bubble seeding by MSTIDs in the ionosphere. Prog Earth Planet Sci 5, 32. https://doi.org/10.1186/s40645-018-0189-2.

Thébault, E., et al. (2015), International geomagnetic reference field: the 12th generation, Earth, Planets and Space, 67 (1), 79, https://doi.org/10.1186/s40623-015-0228-9.

Tran, T. L., Le, H. M., Amory-Mazaudier, C., and Fleury, R. (2017), Climatology of ionospheric scintillation over the Vietnam low-latitude region for the period 2006–2014. Advances in Space Research, 60(8), 1657-1669.

Tsuda, T., M. Yamamoto, H. Hashiguchi, et al. (2016), A proposal on the study of solar-terrestrial coupling processes with atmospheric radars and ground-based observation network, Radio Sci., 51, 1587–1599, 1588–1600, doi:10.1002/2016RS006035.

Tsunoda, R. T. (1981), Time evolution and dynamics of equatorial backscatter plumes, 1, growth phase. J Geophys Res, 86:139.

Tsunoda, R. T. (1985), Control of the seasonal and longitudinal occurrence of equatorial scintillations by the longitudinal gradient in integrated E region Pedersen conductivity. J Geophys Res 90:447.

Tsunoda, R. T. (2005), On the enigma of day-to-day variability in equatorial spread F, Geophys. Res. Lett., 32, L08103, doi:10.1029/2005GL022512.

Tsunoda, R. T. (2008), Satellite traces: An ionogram signature for large scale wave structure and a precursor for equatorial spread F, Geophys. Res. Lett., 35, L20110, doi:10.1029/2008GL035706.

Tsunoda, R. T., Bubenik, D.M., Thampi, S.V., Yamamoto, M. (2010), On large-scale wave structure and equatorial spread F without a post-sunset rise of the F layer. Geophys Res Lett, 37:L07105, doi:10.1029/2009GL042357.

Tsunoda, R.T., Saito, S. & Nguyen, T.T. (2018), Post-sunset rise of equatorial F layer-or upwelling growth?. Prog Earth Planet Sci, 5, 22. https://doi.org/10.1186/s40645-018-0179-4.

Tulasi Ram, S., M. Yamamoto, R. T. Tsunoda, et al. (2014), Characteristics of large-scale wave structure observed from African and Southeast Asian longitudinal sectors, J. Geophys. Res. Space Physics, 119,

1481 doi:10.1002/2013JA019712.
1482 Tulasi Ram, S., K. K. Ajith, T. Yokoyama, M. Yamamoto, and K. Niranjan (2017), Vertical rise velocity of
1483 equatorial plasma bubbles estimated from Equatorial Atmosphere Radar (EAR) observations and HIRB model
1484 simulations, J. Geophys. Res. Space Physics, 122, 6584–6594, doi:10.1002/2017JA024260.
1485 Wan, X., Xiong, C., Rodriguez-Zuluaga, J., et al. (2018): Climatology of the Occurrence Rate and Amplitudes of
1486 Local Time Distinguished Equatorial Plasma Depletions Observed by Swarm Satellite, Journal of Geophysical
1487 Research, Space Physics, 123, 3014–3026, https://doi.org/10.1002/2017JA025072.
1488 Wang, C. (2010). New chains of space weather monitoring stations in China. Space Weather, 8, S08001.
1489 https://doi.org/10.1029/2010SW000603.
1490 Wang, Y., Li, G., Ning, B., et al. (2019). All-Sky Interferometric Meteor Radar Observations of Zonal Structure
1491 and Drifts of Low-Latitude Ionospheric E Region Irregularities, Earth and Space Science, 6, 2653-2662,
1492 https://doi.org/10.1029/2019EA000884.
1493 Wernik, A. W., Secan, J. A., and Fremouw, E. J. (2003), Ionospheric irregularities and scintillation. Advances in
1494 Space Research, 31(4), 971-981.
1495 Woodman, R. F. and La Hoz, C. (1976): Radar observations of F region equatorial irregularities. J. Geophys. Res.,
1496 81, 5447–5466.
1497 Woodman, R. F. (2009): Spread F- an old equatorial aeronomy problem finally resolved?, Ann. Geophys., 27,
1498 1915–1934, https://doi.org/10.5194/angeo-27-1915-2009.
1499 Wu Q (2015), Longitudinal and seasonal variation of the equatorial flux tube integrated Rayleigh-Taylor
1500 instability growth rate. J Geophys Res Space Physics 120:7952–7957. https://doi.org/10.1002/2015JA021553.
1501 Xiao, S.-G., Z. Xiao, J.-K. Shi, et al. (2009), Observational facts in revealing a close relation between acoustic-
1502 gravity waves and midlatitude spread F, J. Geophys. Res., 114, A01303, doi:10.1029/2008JA013747.
1503 Xie H Y, Li G Z, Ning B Q, et al. (2019), The possibility of using all-sky meteor radar to observe ionospheric E-
1504 region field-aligned irregularities. Sci China Tech Sci, 62: 1431–1437, https://doi.org/10.1007/s11431-018-9418-
1505 5.
1506 Xiong, C., Stolle, C., and Lühr, H. (2016), The Swarm satellite loss of GPS signal and its relation to ionospheric
1507 plasma irregularities, Space Weather, 14, 563– 577, doi:10.1002/2016SW001439.
1508 Xu, J. S., J. Zhu, and L. Li (2007), Effects of a major storm on GPS amplitude scintillations and phase fluctuations
1509 at Wuhan in China, Adv. Space Res., 39, 1318– 1324, doi:10.1016/j.asr.2007.03.004.
1510 Xu, Z.-W., J. Wu, and Z.-S. Wu (2004), A survey of ionospheric effects on space based radar, Waves Random
1511 Media, 14, S189– S273.
1512 Yamamoto, M. (2008), Digital beacon receiver for ionospheric TEC measurement developed with GNU
1513 Radio. Earth Planet Sp 60, e21–e24. https://doi.org/10.1186/BF03353137.
1514 Yamamoto, M., Otsuka, Y., Jin, H. et al (2018). Relationship between day-to-day variability of equatorial plasma
1515 bubble activity from GPS scintillation and atmospheric properties from Ground-to-topside model of Atmosphere
1516 and Ionosphere for Aeronomy (GAIA) assimilation. Prog Earth Planet Sci 5, 26. https://doi.org/10.1186/s40645-
1517 018-0184-7.
1518 Yang, Z., and Liu, Z. (2016), Observational study of ionospheric irregularities and GPS scintillations associated
1519 with the 2012 tropical cyclone Tembin passing Hong Kong, J. Geophys. Res. Space Physics, 121, 4705– 4717,
1520 doi:10.1002/2016JA022398.
1521 Yang, Z., & Liu, Z. (2018), Low-latitude ionospheric density irregularities and associated scintillations
1522 investigated by combining COSMIC RO and ground-based Global Positioning System observations over a solar
1523 active period. Journal of Geophysical Research: Space
1524 Physics, 123, 3998– 4014. https://doi.org/10.1029/2017JA024199.
1525 Yeh, K., and Liu, C.-H. (1982), Radio wave scintillations in the ionosphere, Proceedings of the IEEE, 70, 4, 324-
1526 360.
1527 Yizengaw E, Retterer PEE, Roddy P, et al. (2013), Post-midnight bubbles and scintillations in the quiet-time June
1528 solstice. Geophys Res Lett 40. https://doi.org/10.1002/2013GL058307.
1529 Yokoyama, T., Fukao, S., and Yamamoto, M. (2004), Relationship of the onset of equatorial F region
1530 irregularities with the sunset terminator observed with the Equatorial Atmosphere Radar, Geophys. Res. Lett., 31,
1531 L24804, doi:10.1029/2004GL021529.
1532 Yokoyama, T., Yamamoto, M., Otsuka, Y., et al. (2011), On postmidnight low-latitude ionospheric irregularities
1533 during solar minimum: 1. Equatorial Atmosphere Radar and GPS-TEC observations in Indonesia, J. Geophys.
1534 Res., 116, A11325, doi:10.1029/2011JA016797.

Yokoyama, T. (2017), A review on the numerical simulation of equatorial plasma bubbles toward scintillation evaluation and forecasting. Prog Earth Planet Sci 4, 37. https://doi.org/10.1186/s40645-017-0153-6.

Yumoto, K. (2001), Characteristics of Pi 2 magnetic pulsations observed at the CPMN stations: A review of the STEP results. Earth Planet Space, 53, 981–992. https://doi.org/10.1186/BF03351695

Zhang, D. H., Cai, L., Hao, Y. Q., et al. (2010), Solar cycle variation of the GPS cycle slip occurrence in China low-latitude region, Space Weather, 8, S10D10, doi:10.1029/2010SW000583.

Zhou, C., Tang, Q., Huang, F., et al. (2018). The simultaneous observations of nighttime ionospheric E region irregularities and F region medium-scale traveling ionospheric disturbances in midlatitude China. Journal of Geophysical Research: Space Physics, 123, 5195– 5209. https://doi.org/10.1029/2018JA025352.

Zhu, Z., Lan, J., Luo, W., et al. (2015), Statistical characteristics of ionogram spread-F and satellite traces over a Chinese low-latitude station Sanya, 56, 9, 1911-1921, https://doi.org/10.1016/j.asr.2015.03.038.